

REVIEW OF GRAVITATIONAL WAVE DETECTIONS: DYNAMICAL SPACE

Reginald Thomas Cahill

School of Chemical and Physical Sciences, Flinders University, Adelaide 5001, Australia

Received 2014-02-05; Revised 2014-03-17; Accepted 2014-03-27

ABSTRACT

This is a review of the numerous successful gravitational wave detections and the implications for the nature of space and time. The prevailing space time paradigm in physics was founded on the putative “null” results of the Michelson-Morley (MM) 1887 interferometer experiment to detect light speed anisotropy and which resulted in two different new relativity theories: Lorentz relativity (Lorentz, 1904) and special relativity (Einstein, 1905), with the later invoking the claimed reality of space time, in place of separate phenomena of space and time. Miller (1933) repeated the MM experiment in 1925/26 and obtained non-null quality data, resulting in the determination of light speed anisotropy and establishing the key sidereal effect. It is now understood, since 2002, that both of these experiments are consistent and that the MM 1887 experiment was never null: Michelson had used Newtonian physics to calibrate the interferometer. Using Lorentz Relativity, but not Special Relativity, it is now possible to analyse the data from these experiments and which shows that the Michelson interferometer has zero sensitivity unless operated with a dielectric present in the light paths; air in the MM1887 and Miller experiments. Since that 2002 analysis various older and new light speed anisotropy experiments have produced fully consistent results, using different experimental techniques. These have included: RF EM Speeds in coaxial cable, optical fiber Michelson Interferometer, optical fiber/RF coaxial cables, earth spacecraft flyby RF doppler shifts, 1st order dual RF coaxial cables. These are all classical phenomena detectors. However in 2013 nanotechnology quantum detectors were invented that use correlations between electron barrier tunnelling current fluctuations in spatially separated zener diodes. Not only do all of these experiments, spanning 125 years, give a consistent anisotropy velocity, with speed ~ 500 km/s, RA ~ 5 h, Dec. ~ 80 deg S, but all showed significant fluctuations in that velocity. A neo-lorentzian interpretation of these results is that a dynamical 3-space is passing the solar system and exhibits turbulence/wave effects. These wave effects produce gravitational forces and so the experimental data implies that the Michelson and Morley experiment not only detected light speed anisotropy but detected “gravitational waves”. These gravitational waves have properties that are not consistent with the general relativity predicted waves, which travel at the speed of light, are transverse polarised and are weak and only produced by distant major astronomical events. Gravitational waves with these properties have never been detected. The zener diode quantum detectors reveal that quantum fluctuations are not random and intrinsic to a quantum system, but are imposed by the passing space: This discovery has major implications for the interpretations of quantum theory and the quantum to classical transition, which profoundly creates our reality. The dynamical space theory also poses an intrinsic inflation epoch.

Keywords: Gravitational Waves, Light Speed Anisotropy, Dynamical 3-Space, Quantum Classical Transition

1. INTRODUCTION

The experimental data from over 125 years shows that light speed anisotropy and gravitational waves have been repeatedly detected, via a variety of experimental

techniques. Repeated experiments and observations are the hallmark of science. The detected gravitational waves, shown to be turbulence/fluctuations in the dynamical 3-space flow relative to the earth, have significant amplitudes and do not have the characteristics

predicted by General Relativity (GR): Such wave phenomena have never been detected (Cahill, 2005a; 2009b; 2014). Until 2013 the successful experiments used classical detectors, such as the gas-mode Michelson interferometer, but in 2013 the amazing phenomena of nanotechnology quantum detectors was discovered (Cahill, 2013b). This technique uses cheap zener diodes and the data reveals that the quantum barrier electron tunnelling quantum fluctuations are solely caused by fluctuations of the 3-space: This is why the zener diode detectors are so exquisitely sensitive to space flow fluctuations (gravitational waves). This discovery represents a major development in the interpretation and understanding of the nature of quantum phenomena and the quantum fluctuations that manifest in the quantum to classical transition, resulting in the emergent 'classical' world: Localisation of quantum states. So we are seeing a unification of space, gravity and the quantum theories. Here we review the long saga in which an observable and dynamical 3-space was repeatedly overlooked by mainstream physics, despite the many successful experimental detections. In later years many failed experiments used flawed designs, such as vacuum-mode Michelson interferometers and resonant cavities. Not only are gravitational waves now easily and cheaply detected and characterised, but new experimental phenomena caused by the underlying dynamical 3-space may now be studied in simple laboratory experiments.

The prevailing spacetime paradigm in physics was founded on the putative "null" results of the (Michelson and Morley, 1887) interferometer experiment to detect light speed anisotropy and which resulted in two different new relativity theories: Lorentz Relativity (LR), (Lorentz, 1904) and Special Relativity (SR), (Einstein 1905), with the later invoking spacetime, in place of separate phenomena of space and time. Miller in 1925/26 repeated the MM experiment and obtained non-null quality data, resulting in the determination of light speed anisotropy and establishing the key sidereal effect. It is now understood that both of these experiments are consistent and that the 1887 experiment was never null: Michelson had used Newtonian physics to calibrate the interferometer. Using Lorentz relativity, but not special relativity, it is now possible to analyse the data from these experiments and which shows that the Michelson interferometer has zero sensitivity unless operated with a dielectric present in the light paths. A key realisation should be immediately noted: In LR the length contraction effect of a physical object is determined by the speed of the object relative to the

actual space, while in SR the Lorentz contraction effect is determined by the speed relative to an observer and applies to all spatial separations, whether or not an object is present. These very different effects have made it possible to test which contraction effect is observed and it is only LR that agrees with the experimental data (Cahill, 2013a). Indeed SR may be exactly derived from the much older galilean relativity, by a mere choice of space and time coordinates for each observer that renders, wrt these co-ordinates, the invariance of the speed of light. However that is merely a coordinate effect and the observed relativistic effects are dynamical and are described only by neo-Lorentz relativity (Cahill, 2013a). As well the Michelson interferometer has an intrinsic design flaw, unknown to Michelson, in which in vacuum mode the time delay effects caused by the geometry of the interferometer exactly cancel the time variations caused by the actual Lorentz contractions of the interferometer arms. Only with a dielectric present in the light paths is this cancellation effect partially avoided, although with a gas present, such as air, there is still considerable cancellation and the interferometer is extremely insensitive to light speed anisotropy and gravitational waves. This effect was discovered in 2002 by (Cahill and Kitto, 2003). Surprisingly vacuum mode Michelson interferometers continue to be used and developed, at great cost, to detect gravitational waves. Since 2002 various older and new light speed anisotropy experiments have produced fully consistent results, using different experimental techniques. These have included: RF EM speeds in coaxial cable, optical fiber Michelson interferometer, optical fiber/RF coaxial cables, Earth Spacecraft Flyby RF Doppler Shifts, 1st Order Dual RF coaxial cables. These are all classical phenomena detectors. However in 2013 nanotechnology quantum detectors were invented that use correlations between electron barrier tunnelling current fluctuations in spatially separated zener diodes operating in reverse bias mode. Not only do all of these experiments, spanning 125 years, give a consistent anisotropy velocity, with 3-space speed ~ 500 km/s, from the direction RA ~ 5 h, Dec. ~ 80 deg S, but all showed significant fluctuations in that velocity. A neo-Lorentzian interpretation of these results is that a dynamical 3-space is passing the solar system and exhibits turbulence/wave effects. These wave effects produce gravitational forces and so the experimental data implies that the Michelson-orley 1887 experiment not only detected light speed anisotropy but also detected "gravitational waves". These gravitational waves have

properties that are not consistent with the general relativity predicted waves, which travel at the speed of light, are transverse polarised and are weak and only produced by distant major astronomical events. Gravitational waves with these properties have never been detected.

The zener diode quantum detectors reveal that quantum fluctuations are not random and intrinsic to a quantum system, but are imposed by the passing space: This discovery has major implications for the interpretations of quantum theory and the quantum to classical transition, which profoundly creates our reality, namely the spatial localisation of quantum systems which are intrinsically a wave phenomena. A remarkable realisation is that zener diode detectors have been operating and systematically collecting space fluctuation data for some 15 years and are known as Random Event Generators (REG) and operated within the context of the Global Consciousness Project (GCP). That data is of extreme significance, with the recorded data being taken every 1 sec by some 60 detectors located around the world. This data permits the study of correlations between significant space flow disturbances and subsequent solar flares, correlations with earthquakes, localised correlations with solar eclipses and recently the detection of gravitational waves produced by earth vibrations. As well it has been possible to revisit gravitational wave data from the Weber and (Amaldi *et al.*, 1981a; 1981b) resonant mass gravitational wave detectors. We also note that the dynamical space also posses an intrinsic inflation epoch, which in GR is introduced by means of an *ad hoc* inflation field.

1.2. Michelson Interferometer Detectors

The Michelson interferometer was a brilliantly conceived instrument for measuring light speed anisotropy. However Michelson made two critically incorrect assumptions, which inadvertently had the effect of misguiding physics for another 100 years and more. The 1st was to assume Newtonian physics in determining the calibration theory for the instrument and the 2nd was to average data from successive days at the same approximate times, with the assumption being that this would average out “instrumental fluctuations”, when it had the opposite effect because there were significant “gravitational wave” effects in the data and these were different on different days, even at the same time.

We now have a clear understanding of the design principles of the Michelson interferometer as a detector of light speed anisotropy and ipso facto as a detector for the actual 3- space flow turbulence/gravitational waves, (Cahill and Kitto, 2003; Cahill, 2005b). This is because

two different and independent effects exactly cancel in vacuum mode. The key insight is that the dynamical space is describable at a macroscopic/classical level by a detectable velocity field $v(r, t)$, relative to an observer using spatial coordinate r and time coordinate t , both of which must be carefully determined so as to remove absolute motion effects, that is, effects caused by the motion of rods and clocks wrt space. The key aspects of the interferometer are shown in **Fig. 1**. Taking account of the geometrical path differences, the Fitzgerald-Lorentz arm-length contraction and the Fresnel drag effect leads to the travel time difference between the two arms and which is detected by interference effects (The dielectric of course does not cause the observed effect, it is merely a necessary part of the instrument design physics, just as mercury in a thermometer does not cause temperature), is given by Equation 1:

$$\Delta t = k^2 \frac{Lv^2 p}{c^3} \cos(2(\theta - \psi)) \tag{1}$$

where, ψ specifies the direction of $v(r, t)$ projected onto the plane of the interferometer, giving projected speed v_p , relative to the local meridian and where $k^2 = (n^2 - 2)(n^2 - 1)$, with n the refractive index. Neglect of the absolute motion relativistic Fitzgerald-Lorentz contraction effect gives $k^2 \approx n^3 \approx 1$ for gases, which is essentially the Newtonian theory that Michelson used.

We derive the calibration constant k^2 for the Michelson interferometers in the case of Lorentzian relativity. The two arms are constructed to have the same lengths when they are physically parallel to each other. For convenience assume that the value L_0 of this length refers to the lengths when at rest wrt space The Fitzgerald-Lorentz effect is that the arm AB parallel to the direction of motion is shortened to Equation 2:

$$L_{\parallel} = L_0 \sqrt{1 - \frac{v_R^2}{c^2}} \tag{2}$$

where, v_R is the lengthwise speed of the arm relative to space. In SR v_R is the speed relative to the observer, who is presumably at rest wrt the arms, then $v_R = 0$ and there is no arm contraction effect.

For later reference we also give the time dilation expression for physical clocks Equation 3:

$$\tau = T \sqrt{1 - \frac{v_R^2}{c^2}} \tag{3}$$

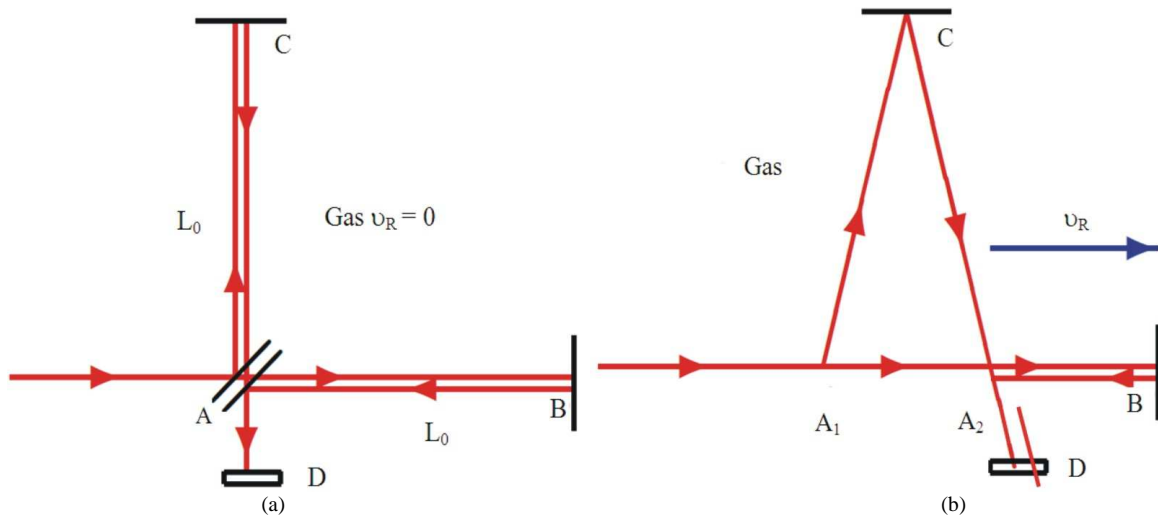


Fig. 1. Schematic diagrams of the gas-mode Michelson Interferometer, with beam splitter/mirror at A and mirrors at B and C. Corresponding Author: Mounted on arms from A, with the arms of equal length L_0 when at rest. D is the detector screen. In (a) the interferometer is at rest in space. In (b) the instrument and gas are moving through 3-space with speed v_R parallel to the AB arm. Interference fringes are observed at D when mirrors B and C are not exactly perpendicular—the Hick’s effect. As the interferometer is rotated in the plane shifts of these fringes are seen in the case of absolute motion, but only if the apparatus operates in a gas. By measuring fringe shifts the speed v_R may be determined

where, τ is the elapsed time given by the clock, for an actual time interval T.

For simplicity here we take the motion of the detector to be parallel to the arm AB. Following **Fig. 1** let the time taken for light to travel from A \rightarrow B be t_{AB} and that from B \rightarrow A be t_{BA} , where V is the speed of light relative to the gas, which is moving with the detector. We shall also neglect the Fresnel drag effect, so $V = c/n$. Then Equation 4:

$$Vt_{AB} = L_{\parallel} + v_R t_{AB} \text{ and } Vt_{BA} = L_{\parallel} - v_R t_{BA}$$

$$t_{ABA} = t_{AB} + t_{BA} = \frac{L_{\parallel}}{V - v_R} + \frac{L_{\perp}}{V + v_R} = \frac{2L_0V\sqrt{1 - \frac{v_R^2}{c^2}}}{V^2 - v_R^2} \quad (4)$$

For the other arm, with no contraction in its length:

$$(Vt_{AC})^2 = L_0^2 + (v_R t_{AC})^2$$

$$t_{AC} = \frac{L_0}{\sqrt{V^2 - v_R^2}}, \quad t_{ACA} = 2t_{AC} = \frac{2L_0}{\sqrt{V^2 - v_R^2}} \quad (5)$$

Giving finally for the travel time difference for the two arms:

$$\Delta t = \frac{2L_0V\sqrt{1 - \frac{v_R^2}{c^2}}}{V^2 - v_R^2} - \frac{2L_0}{\sqrt{V^2 - v_R^2}} \quad (6)$$

Now trivially $\Delta t = 0$ if $v_R = 0$, but also $\Delta t = 0$ when $v_R \neq 0$ but only if $V = c$, viz vacuum. This then would result in a null result on rotating the apparatus. Hence the null result of the Michelson apparatus is only for the special case of light travelling in vacuum. However if the apparatus is immersed in a gas then $V < c$ and a non-null effect is expected on rotating the apparatus, since now $\Delta t \neq 0$. It is essential then in analysing data to correct for this refractive index effect. Putting $V = c/n$ in (6) we find, for $v_R \ll V$ and when $n \approx 1$, that Equation 7:

$$\Delta t = n(n^2 - 1)\frac{L_0v_R^2}{c^3} \quad (7)$$

However if the data is analysed not using the Fitzgerald-Lorentz contraction (2), then, as done in the old analyses, the estimated time difference is Equation 8:

$$\Delta t = \frac{2L_0V}{v^2 - v_R^2} - \frac{2L_0}{\sqrt{V^2 - v_R^2}} \quad (8)$$

Which again for $v_R \ll V$ gives Equation 9:

$$\Delta t = n^3 \frac{L_0 v_R^2}{c^3} \tag{9}$$

With Fresnel drag and $n \approx 1$ the sign of Δt is reversed. Symmetry arguments easily show that when rotated we obtain a $\cos(2\theta)$ factor.

However the above analysis does not correspond to how the interferometer is actually operated. That analysis does not actually predict fringe shifts, for the field of view would be uniformly illuminated and the observed effect would be a changing level of luminosity rather than fringe shifts. As Michelson and Miller knew, the mirrors must be made slightly non-orthogonal with the degree of non-orthogonality determining how many fringe shifts were visible in the field of view. Experimenting with this effect determines a comfortable number of fringes: Not too few and not too many. The non-orthogonality reduces the symmetry of the device and instead of having period of 180 the symmetry now has a period of 360°, so that we must add the extra term $a \cos(\theta - \beta)$ in Equation 10:

$$\Delta t = k^2 \frac{L(1 + e\theta) v_p^2}{c^3} \cos(2(\theta - \psi)) + a(1 + e\theta) \cos(\theta - \beta) + f \tag{10}$$

The factor $1 + e\theta$ models the temperature effects, namely that as the arms are uniformly rotated, one rotation taking several minutes, there will be a temperature induced change in the length of the arms. If the temperature effects are linear in time, as they would be for short time intervals, then they are linear in θ . In the non-orthogonality term the parameter a is proportional to the length of the arms and so also has the temperature factor. The term f simply models any set effect. Michelson and Morley and Miller took these two effects into account when analysing his data.

The interferometers are operated with the arms horizontal. Then θ is the azimuth of one arm relative to the local meridian, while ψ is the azimuth of the absolute motion velocity projected onto the plane of the interferometer, with projected component v_p . Here the Fitzgerald-Lorentz contraction is a real dynamical effect of absolute motion, unlike the Einstein spacetime view that it is merely a spacetime perspective artifact and whose magnitude depends on the choice of observer. The instrument is operated by rotating at a rate of one rotation over several minutes and observing the shift in the fringe

pattern through a telescope during the rotation. Then fringe shifts from six (Michelson and Morley, 1987) or twenty (Miller) successive rotations are averaged to improve the signal to noise ratio and the average sidereal time noted. Some examples are shown in **Fig. 2** and illustrate the incredibly clear signal. The ongoing claim that the Michelson-Morley experiment was a null experiment is disproved. **Fig. 3** shows data from these two experiments over a 24 h sidereal day. The large fluctuations are gravitational wave effects and have been seen in all experiments that detected light speed anisotropy.

1.3. Dewitte RF Coaxial Cable Detector

The enormously significant 1991 DeWitte double one-way 1st order in v/c experiment successfully measured the anisotropy of the speed of RF EM waves using clocks at each end of the RF coaxial cables (Cahill, 2006e; 2012b). The technique uses rotation of the coaxial cables, by means of the earth rotation, to permit extraction of the EM speed anisotropy, despite the clocks not being synchronised. Data from this 1st order in v/c experiment agrees with the speed and direction of the anisotropy results from all the other experiments reported herein.

Figure 4 shows the arrangement for measuring the one-way speed of light, either in vacuum, a dielectric, or RF coaxial cable. It is usually argued that one-way speed of light measurements are not possible because the clocks C_1 and C_2 cannot be synchronised. However this is false. An important effect that needs to be included is the clock offset effect caused by transport, when the apparatus is rotated in this case, but most significantly the Fresnel drag effect is not present in RF coaxial cables, at low RF frequencies. In **Fig. 4** the actual travel time $t_{AB} = t_B - t_A$ from A to B, as distinct from the clock indicated travel time $T_{AB} = T_B - T_A$, is determined by Equation 11:

$$V(v \cos(\theta)) t_{AB} = L + v \cos(\theta) t_{AB} \tag{11}$$

where, the 2nd term comes from the end B moving an additional distance $v \cos(\theta) t_{AB}$ during time interval t_{AB} . With Fresnel $V(v) = \frac{c}{n} + v \left(1 - \frac{1}{n^2}\right)$ drag when V and v are parallel and where n is the dielectric refractive index. Then Equation 12:

$$t_{AB} = \frac{L}{V(v \cos(\theta)) - v \cos(\theta)} = \frac{nL}{c} + \frac{v \cos(\theta) L}{c^2} + .. \tag{12}$$

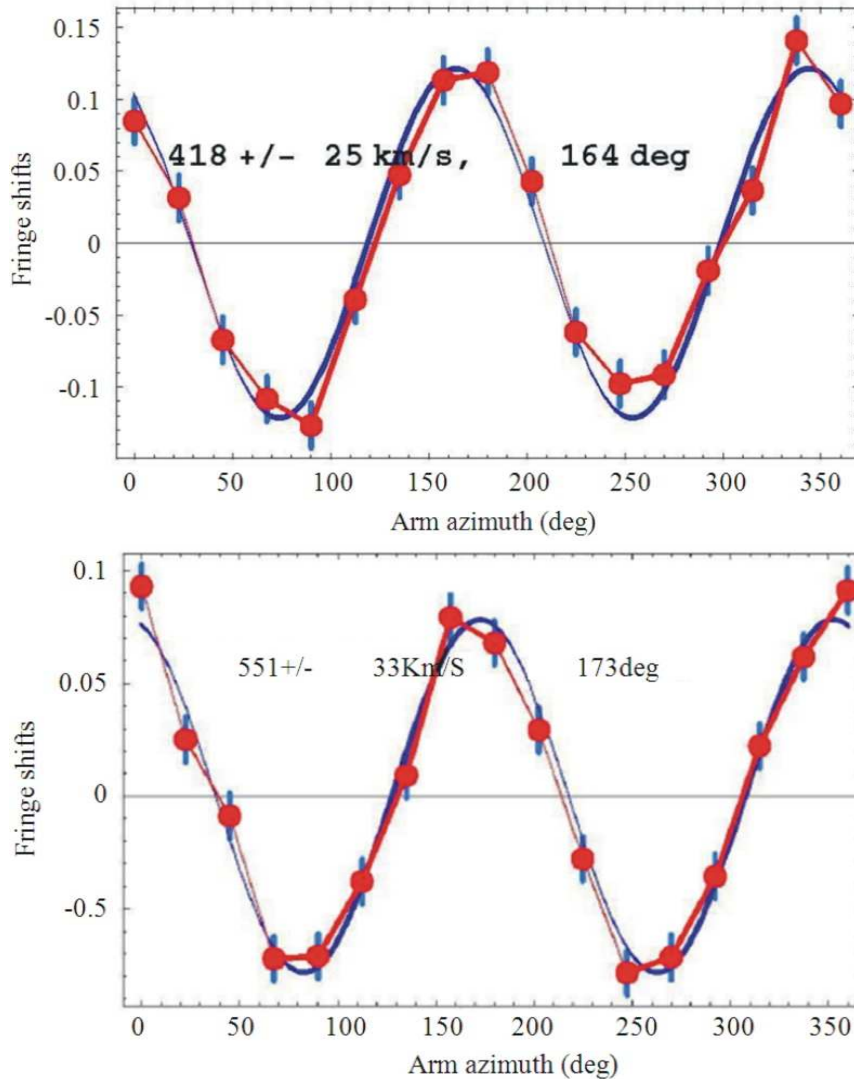


Fig. 2. Top: Typical Miller data from 1925/26 gas-mode Michelson interferometer, from averaging 20 360° rotations, (Miller, 1933). Bottom: Data from Michelson-Morley 1887 gas-mode interferometer, from averaging 6 360° rotations. In both plots the nonorthogonal term and temperature drift effects have been removed from the data, after a least squares best fit using the full detector theory derived in the text, (10), (Michelson and Morley, 1887). This reduced data then shows an impressive agreement with the $\cos(2(\theta\psi))$ form

However if there is no Fresnel drag effect, $V = c/n$, as is the case in RF coaxial cables, then we obtain Equation 13:

$$t_{AB} = \frac{L}{V(v\cos(\theta)) - v\cos(\theta)} = \frac{nL}{c} + \frac{v\cos(\theta)Ln^2}{c^2} + \dots \quad (13)$$

It would appear that the two terms in (12) or (13) can be separated by rotating the apparatus, giving the magnitude and direction of v . However it is $T_{AB} = T_B -$

T_A that is measured and not t_{AB} , because of an unknown fixed clock offset τ , as the clocks are not a priori synchronised and as well an angle dependent clock transport offset $\Delta\tau$, at least until we can establish clock synchronisation, as explained below.

Then the clock readings are $T_A = t_A$ and $T_B = t_B + \tau$ and $T'_B = t'_B + \tau + \Delta\tau$, where $\Delta\tau$ is a clock offset that arises from slowing of clock C_2 as it is transported during the rotation through angle $\Delta\theta$, see **Fig. 4**.

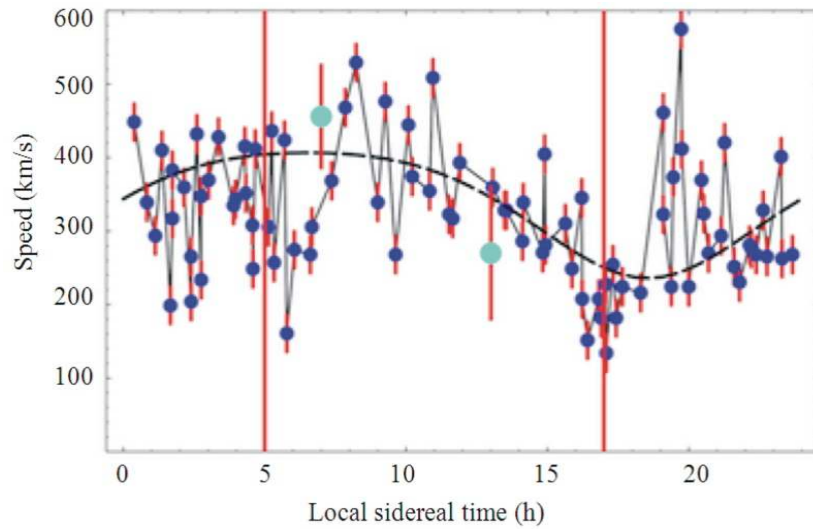


Fig. 3. Speeds v_p , of the 3-space velocity v projected onto the horizontal plane of the Miller gas-mode Michelson interferometer located atop Mt. Wilson, plotted against local sidereal time in hours, for a composite day, with data collected over a number of days in September 1925. The data shows considerable fluctuations, from hour to hour and also day to day, as this is a composite day. The dashed curve shows the non-fluctuating best-fit variation over one day, as the earth rotates, causing the projection onto the plane of the interferometer of the velocity of the average direction of the space flow to change. The maximum projected speed of the curve is 417 km/s (using the STP air refractive index of $n = 1.00029$ and the min/max occur at approximately 5 and 17 h local sidereal time (Right Ascension). Note that the Cassini flyby in August gives a RA= 5.15 h, close to the RA apparent in the above plot. The green data points, with error bars, at 7 and 13 h are from the Michelson- Morley 1887 data, from averaging (excluding only the July 8 data for 7 h because it has poor S/N). The fiducial time lines are at 5 and 17 h. The speed fluctuations are seen to be much larger than the statistically determined errors, confirming the presence of turbulence in the 3-space flow, i.e., gravitational waves, as first seen in the Michelson-Morley experiment

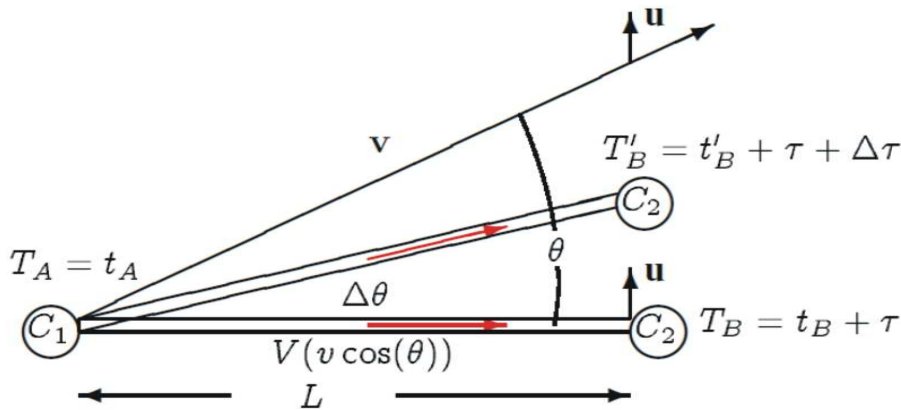


Fig. 4. Schematic layout for measuring the one-way speed of light in either free-space, optical fibers or RF coaxial cables, without requiring the synchronisation of the clocks C_1 and C_2 . Here τ is the, initially unknown, offset time between the clocks. Times t_A and t_B are true times, without clock offset and clock transport effects, while $T_A = t_A$, $T_B = t_A + \tau$ and $T'_B = t'_B + \tau + \Delta\tau$ are clock readings. $V (v \cos(\theta))$ is the speed of EM radiation wrt the apparatus before rotation and $V (v \cos(\theta - \Delta\theta))$ after rotation, v is the velocity of the apparatus through space in direction θ relative to the apparatus before rotation, u is the velocity of transport for clock C_2 and $\Delta\tau < 0$ is the net slowing of clock C_2 from clock transport, when apparatus is rotated through angle $\Delta\theta > 0$. Note that $v, u > 0$

The clock transport offset $\Delta\tau$ follows from the clock motion effect (Cahill, 2012b) Equation 14:

$$\Delta\tau = dt\sqrt{1 - \frac{(v+u)^2}{c^2}} - dt\sqrt{1 - \frac{v^2}{c^2}} = -dt\frac{v.u}{c^2} + \dots, \quad (14)$$

When clock C_2 is transported at velocity u over time interval dt , compared to C_1 . Now $v.u = vu \sin(\theta)$ and $dt = L\Delta\theta/u$. Then the change in T_{AB} from this small rotation is, using (13) for the case of no Fresnel drag Equation 15:

$$\Delta T_{AB} = -\frac{v \sin(\theta) L n^2 \Delta\theta}{c^2} + \frac{v \sin(\theta) L \Delta\theta}{c^2} + \dots \quad (15)$$

As the clock transport effect appears to make the clock-determined travel time longer (2nd term). Integrating we get Equation 16:

$$T_B - T_A = \frac{nL}{c} + \frac{v \cos(\theta) L (n^2 - 1)}{c^2} + \tau \quad (16)$$

where, τ is now the constant offset time. The $v \cos(\theta)$ term may be separated by means of the angle dependence. Then the value of τ may be determined and the clocks synchronised. However if the propagation medium is liquid, or dielectrics such as glass and optical fibers, the Fresnel drag effect is present and we then use (12) and not (13). Then in (16) we need make the replacement $n \rightarrow 1$ and then the 1st order in v/c term vanishes. However, in principle, separated clocks may be synchronised by using RF coaxial cables.

The DeWitte $L = 1.5$ km 5 MHz RF coaxial cable experiment, in Brussels in 1991 (Cahill, 2006d; 2012b), was a double 1st order in v/c detector, using the scheme in Fig. 4, but employing a 2nd RF coaxial cable for the opposite direction, giving clock difference $T_C - T_D$, to cancel temperature effects and also used 3 Caesium atomic clocks at each end. The orientation was NS and rotation was achieved by that of the earth. Then Equation 17:

$$T_{AB} - T_{CD} = \frac{2v \cos(\theta) L (n^2 - 1)}{c^2} + 2\tau \quad (17)$$

For a horizontal detector the dynamic range of $\cos(\theta)$ is $2 \sin(\lambda) \cos(\delta)$, caused by the earth rotation, where λ is the latitude of the detector location and δ is the declination of v . The value of τ may be determined and the clocks synchronised. Some of DeWitte's data and

results are in Fig. 5 and 6. We see that DeWitte's RF EM speed anisotropy experiment is consistent with other experiments and also shows significant fluctuations.

1.4. Earth Flyby RF Doppler Shifts: 3-Space Flow

The motion of spacecraft relative to the earth are measured by observing the direction and Doppler shift of the transponded RF EM transmissions. This gives another technique to determine the speed and direction of the dynamical 3-space as manifested by the light speed anisotropy (Cahill, 2009c). The repeated detection of the anisotropy of the speed of light has been, until recently, ignored in analysing the Doppler shift data, causing the long-standing anomalies in the analysis (Anderson *et al.*, 2008). The use of the Minkowski-Einstein choice of time and space coordinates does not permit the analysis of these Doppler anomalies, as they mandate that the speed of the EM waves be invariant.

Because we shall be extracting the earth inflow effect we need to take account of a spatially varying, but not timevarying, 3-space velocity. In the earth frame of reference, see Fig. 7 and using clock times from earth-based clocks, let the transmitted signal from earth have frequency f . The time for one RF maximum to travel distance D to SC from earth is, see Fig. 8 Equation 18:

$$t_1 = \int_0^D \frac{dr}{c - v_i(r)} \quad (18)$$

The next RF maximum leaves time $T = 1/f$ later and arrives at SC at time, taking account of SC motion Equation 19:

$$t_2 = T + \int_0^{D-vT} \frac{dr}{c - v_i(r)} \quad (19)$$

The period at the SC of the arriving RF is then Equation 20:

$$T' = t_2 - t_1 = T + \int_D^{D-vT} \frac{dr}{c - v_i(r)} \approx \frac{c - v_i(D) - V}{c - v_i(D)} T \quad (20)$$

Essentially this RF is reflected (In practice a more complex protocol is used) by the SC. Then the 1st RF maximum takes time to reach the earth Equation 21:

$$t_1' = -\int_D^0 \frac{dr}{c + v_i(r)} \quad (21)$$

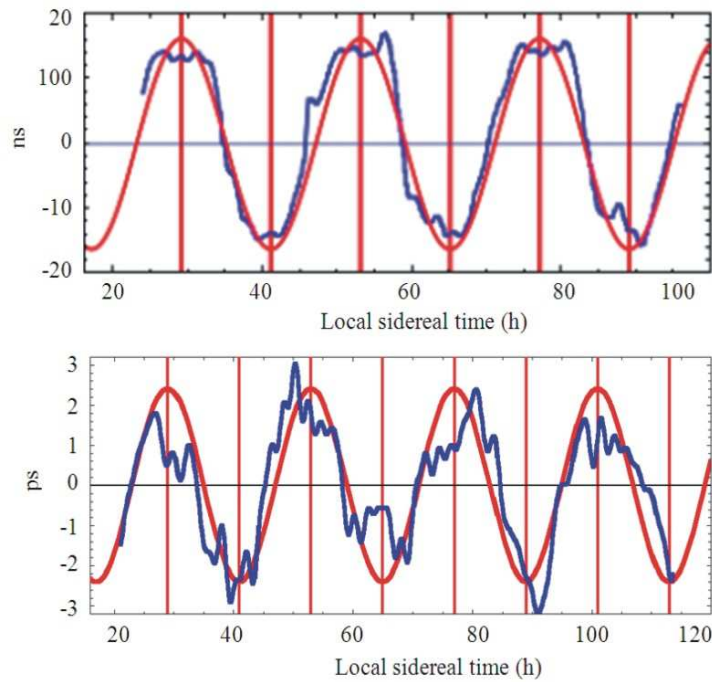


Fig. 5. Top: Data from the 1991 DeWitte NS RF coaxial cable experiment, $L = 1.5$ km, using the arrangement shown in **Fig. 4**, with a 2nd RF coaxial cable carrying a signal in the reverse direction. The vertical red lines are at $RA = 5^h$. DeWitte gathered data for 178 days and showed that the crossing time tracked sidereal time and not local solar time, see **Fig. 6**. DeWitte reported that $v \approx 500$ km/s. If the full fresnel drag effect is included no effect would have been seen. Bottom: Dual RF coaxial cable detector data from May 2009 using the technique in **Fig. 15** with $L = 20$ m. NASA spacecraft doppler shift data predicts $Dec. = -77^\circ$, $v = 480$ km/s, giving a sidereal dynamic range of 5.06 ps, very close to that observed. The vertical red lines are at $RA = 5^h$. In both data sets we see the earth sidereal rotation effect together with significant wave/turbulence effects

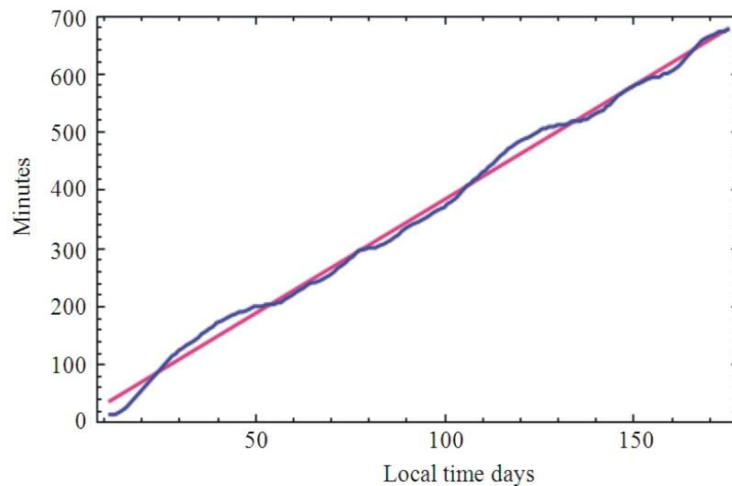


Fig. 6. DeWitte collected data over 178 days and demonstrated that the zero crossing time, see **Fig. 5**, tracked sidereal time and not local solar time. The plot shows the negative of the drift in the crossing time vs local solar time and has a slope, determined by the bestfit straight line, of -3.918 min per day, compared to the actual average value of -3.932 min per day, the difference between a sidereal day and a solar day

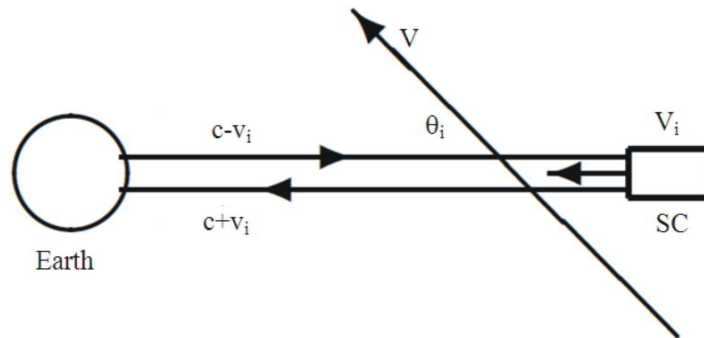


Fig. 7. Asymptotic flyby configuration in earth frame-of-reference, with Spacecraft (SC) approaching Earth with velocity V_i . The departing asymptotic velocity will have a different direction but the same speed, as no force other than conventional Newtonian gravity is assumed to be acting upon the SC. The dynamical 3-space velocity is $v(r; t)$, though taken to be time independent during the Doppler shift measurement, which causes the outward EM beam to have speed $c-v_i(r)$ and inward speed $c+v_i(r)$, where $v_i(r) = v(r) \cos(\theta_i)$, with θ_i the angle between v and V . A similar description applies to the departing SC, labeled $i \rightarrow f$

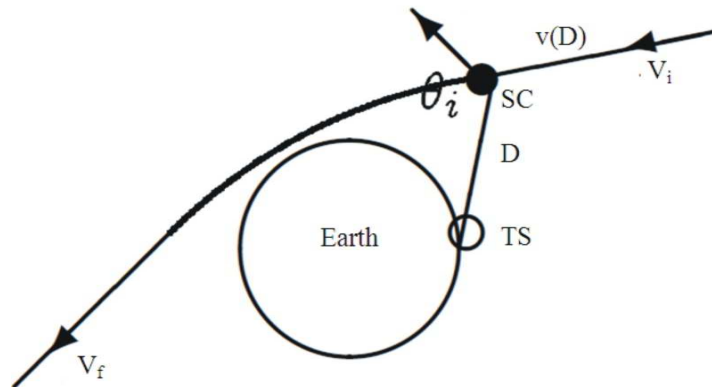


Fig. 8. Spacecraft (SC) earth flyby trajectory, with initial and final asymptotic velocity V , differing only by direction. The Doppler shift is determined from **Fig. 7** and (31). The 3-space flow velocity at the location of the SC is v . The line joining Tracking Station (TS) to SC is the path of the RF signals, with length D . As SC approaches earth $v(D)$ changes direction and magnitude and hence magnitude of projection $v_i(D)$ also changes, due to earth component of 3-space flow and also because of RF direction to/from tracking station. The SC trajectory averaged magnitude of this earth in-flow is determined from the flyby data and compared with theoretical prediction

And the 2nd RF maximum arrives at the later time
Equation 22:

$$t_1' = T' - \int_{D-VT'}^0 \frac{dr}{c + v_i(r)} \quad (22)$$

Then the period of the returning RF at the earth is
Equation 23 to 25:

$$T'' = t_2' - t_1' \quad (23)$$

$$= T' + \int_D^{D-VT'} \frac{dr}{c + v_i(r)} \quad (24)$$

$$\approx \frac{c + v_i(D) - V}{c + v_i(D)} T' \quad (25)$$

Then overall we obtain the return frequency to be
Equation 26:

$$f'' = \frac{1}{T''} \approx \frac{c + v_i(D)}{c + v_i(D) - V} \frac{c - v_i(D)}{c - v_i(D) - V} f \quad (26)$$

Ignoring the projected 3-space velocity $v_i(D)$, that is, assuming that the speed of light is invariant as per the usual literal interpretation of the Einstein (1905) light speed postulate, we obtain instead Equation 27:

$$f'' = \frac{c^2}{(c-V)^2} f \tag{27}$$

The use of (27) instead of (26) is the origin of the putative anomalies. Expanding (27) we obtain Equation 28:

$$\frac{\Delta}{f} = \frac{f'' - f}{f} = \frac{2V}{c} \tag{28}$$

However expanding (26) we obtain, for the same Doppler shift Equation 29:

$$\frac{\Delta}{f} = \frac{f'' - f}{f} = \left(1 + \frac{v(D)^2}{c^2}\right) \frac{2V}{c} \tag{29}$$

It is the prefactor to $2V/c$ missing from (28) that explains the spacecraft Doppler anomalies and also permits yet another determination of the 3-space velocity $v(D)$ at the location of the SC. The published data does not give the Doppler shifts as a function of SC location, so the best we can do at present is to use a SC trajectory-averaged $v(D)$, namely \bar{v}_i and \bar{v}_f , for the incoming and outgoing trajectories, as further discussed below.

From the observed Doppler shift data acquired during a flyby and then best fitting the trajectory, the asymptotic hyperbolic speeds $V_{i\infty}$ and $V_{f\infty}$ are inferred from (28), but incorrectly so, as in (Anderson *et al.*, 2008). These inferred asymptotic speeds may be related to an inferred asymptotic Doppler shift Equation 30:

$$\frac{\Delta f_{i\infty}}{f} = \frac{f'_{i\infty} - f}{f} = \frac{2V_{i\infty}}{c} \tag{30}$$

Which from (29) gives Equation 31:

$$V_{i\infty} \equiv \frac{\Delta f_{i\infty}}{f} \cdot \frac{c}{2} = \left(1 + \frac{\bar{v}_i^2}{c^2}\right) V \tag{31}$$

where, V is the actual asymptotic speed. Similarly after the flyby we obtain Equation 32:

$$V_{f\infty} \equiv \frac{\Delta f_{f\infty}}{f} \cdot \frac{c}{2} = \left(1 + \frac{\bar{v}_f^2}{c^2}\right) V \tag{32}$$

And we see that the ‘‘asymptotic’’ speeds $V_{i\infty}$ and $V_{f\infty}$ must differ, as indeed reported in (Anderson *et al.*,

2008). We then obtain the expression for the so-called flyby anomaly Equation 33:

$$\Delta V_{\infty} = V_{f\infty} - V_{i\infty} = \frac{\bar{v}_f^2 - \bar{v}_i^2}{c^2} \tag{33}$$

where, here $V \approx V_{\infty}$ to sufficient accuracy, where V_{∞} is the average of $V_{i\infty}$ and $V_{f\infty}$. The existing data on v permits ab initio predictions for ΔV_{∞} . As well a separate leastsquares- fit to the individual flybys permits the determination of the average speed and direction of the 3-space velocity, relative to the earth, during each flyby. These results are all remarkably consistent with the data from the various laboratory experiments that studied v . We now indicate how \bar{v}_i and \bar{v}_f were parametrised during the best-fit to the flyby data. $v_{galactic} + v_{sun} - v_{orbital}$ is taken as constant during each individual flyby, with v_{sun} inward towards the sun, with value 42 km/s and $v_{orbital}$ as tangential to earth orbit with value 30 km/s -consequentially the directions of these two vectors changed with day of each flyby. This linear superposition is only approximate (Cahill, 2009a). The earth inflow v_{earth} was taken as radial and of an unknown fixed trajectory-averaged value. So the averaged direction but not the averaged speed varied from flyby to flyby, with the incoming and final direction being approximated by the (a_i, δ_i) and (a_f, δ_f) asymptotic directions shown in **Table 1**. The predicted theoretical variation of $v_{earth}(R)$ is shown in **Fig. 9**. To best constrain the fits to the data the flyby data was used in conjunction with the RA from the Krisher optical fiber data, (Krisher *et al.*, 1990). This results in the plot in **Fig. 11**, the various flyby data in **Table 1** and the earth in-flow speed determination in **Fig. 10**. The results are in remarkable agreement with the results from Miller, showing the extraordinary skill displayed by Miller in carrying out his massive interferometer experiment and data analysis in 1925/26. The only effect missing from the Miller analysis is the spatial in-flow effect into the sun, which affected his data analysis. Miller obtained a galactic flow direction of $a = 4.52$ h, $\delta = -70.5^\circ$, compared to that obtained herein from the NASA data of $a = 4:29$ h, $\delta = -75.0^\circ$, which differ by only $\approx 5^\circ$.

As well the flyby Doppler shifts show considerable fluctuations. We conjecture that these are gravitational wave effects, although no analysis has been done to characterise these fluctuations.

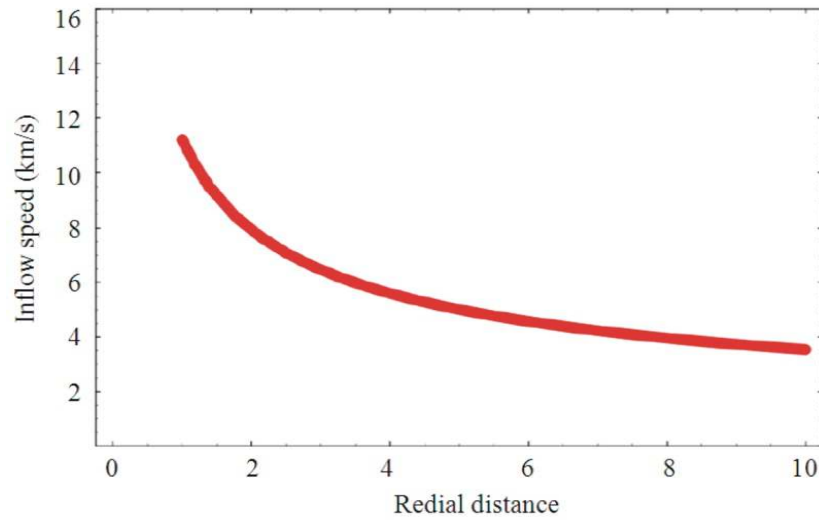


Fig. 9. Predicted Earth 3-space inflow speed Vs distance from earth in earth radii $v = \sqrt{2GM / R}$, plotted only for $R > 1.0$. Combining the NASA/JPL optical fiber RA determination and the flyby Doppler shift data has permitted the determination of the angle- and distance-averaged inflow speed, to be 12.4 ± 5 km/s, see **Fig. 10**

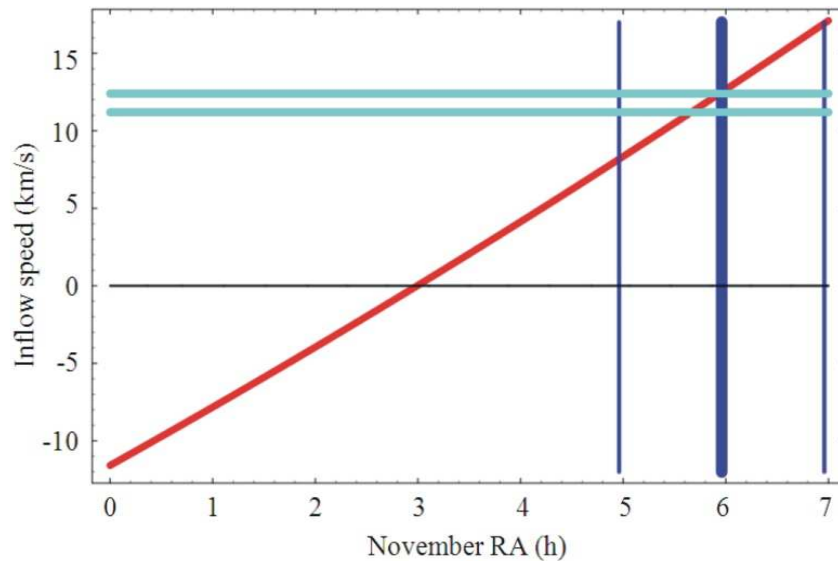


Fig. 10. The weighted angle- and distance-averaged earth 3-space inflow speed v_{earth} , see **Fig. 9**, as determined from NASA data, upper green plot. Uses the averaged Right Ascension from the Krisher *et al.* (1990) data for November, $\alpha = 4.96\text{h}$, but corrected to $\alpha = 6.09\text{h}$ for orientation effect of the optical fiber, shown by the thick blue line, with uncertainty range from wave effects shown by two thin blue lines, compared with the predicted RA from fitting the flyby data, as shown in **Fig. 11**. The red plot shows that prediction for various averaged inflow speeds, with +ve speeds being an inflow, while -ve speeds are an outflow. The earth flyby aberration fits for $v_{\text{earth}} = 0, +4.0, +8.0$ and $+12.4 \text{ km s}^{-1}$ are shown in **Fig. 11**. Theory gives that the inflow speed is $+11.2 \text{ km s}^{-1}$ at the earth's surface-shown by lower green plot. So the detected averaged inflow speed seems to be in good agreement with an expected averaged value. This is the first detection of the earth's spatial inflow and the acceleration of this flow is responsible for the earth's gravity. Note that the flyby data clearly mandates an inflow (+ve values in this figure and not an out-flow-having-ve values)

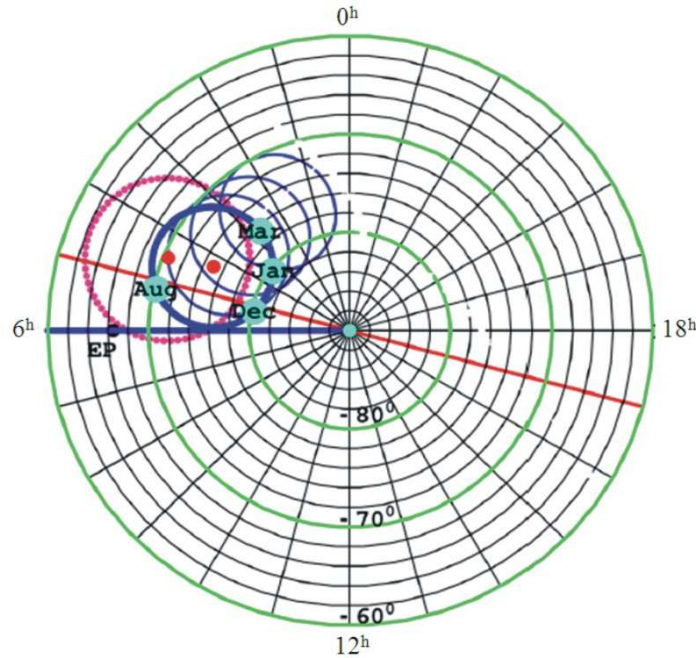


Fig. 11. South celestial pole region. The dot (red) at RA = 4.3 h, Dec. = 75°S and with speed 486 km/s, is the direction of motion of the solar system through space determined from NASA spacecraft earth-fly by Doppler shifts, revealing the EM radiation speed anisotropy. The thick (blue) circle centred on this direction is the observed velocity direction for different days of the year, caused by earth orbital motion and sun 3-space inflow. The corresponding results from the Miller gas-mode interferometer are shown by 2nd dot (red) and its aberration circle (red dots). For December 8, 1992, the velocity is RA = 5.2 h, Dec. = 80°S, speed 491 km/s, see **Table 1**. The thinner blue aberration circles relate to determination of earth 3-space inflow speed

Table 1. Earth flyby parameters from Anderson (1980), for spacecraft Galileo (GLL: flybys I and II), NEAR, Cassini, Rosetta and MESSENGER (M'GER). V_1 is the average osculating hyperbolic asymptotic speed, α and δ are the right ascension and declination of the incoming (i) and outgoing (f) osculating asymptotic velocity vectors and (O) ΔV_∞ is the putative “excess speed” anomaly deduced by assuming that the speed of light is isotropic in modeling the Doppler shifts, as in (30). The observed (O) ΔV_∞ values are from Anderson (1980) and after correcting for atmospheric drag in the case of GLL-II and thruster burn in the case of Cassini. (P) ΔV_∞ is the predicted “excess speed”, after least-squares best-fitting that data using (33): α_v and δ_v and v are the right ascension, declination and the 3-space flow speed for each flyby date, which take account of the earth-orbit aberration and earth inflow effects and correspond to a galactic flow with $\alpha = 4.29h$, $\delta = -75.0^\circ$ and $v = 486$ km/s in the solar system frame of reference. $\Delta\theta$ is the error, in the best fit, for the aberration determined flow direction, from the nearest flyby flow direction. In the fitting the MESSENGER data is not used, as the data appears to be anomalous

Parameter	GLL-I	GLL-II	NEAR	Cassini	Rosetta	M'GER
Date	Dec. 8, 1990	Dec. 8, 1992	Jan. 23, 1998	Aug. 18, 1999	Mar. 4, 2005	Aug. 2, 2005
V_∞ km/s	8.949	8.877	6.851	16.010	3.863	4.056
α_i deg	266.76	219.35	261.17	334.31	346.12	292.61
δ_i deg	-12.52	-34.26	-20.76	-12.92	-2.81	31.44
α_f deg	219.97	174.35	183.49	352.54	246.51	227.17
δ_f deg	-34.15	-4.87	-71.96	-4.99	-34.29	-31.92
α_v h	5.23	5.23	3.44	5.18	2.75	4.89
δ_v deg	-80.3	-80.3	-80.3	-70.3	-76.6	-69.5
v km/s	490.6	490.6	497.3	478.3	499.2	479.2
(O) ΔV_∞ mm/s	3.92±0.3	-4.6±1.0	13.46±0.01	-2±1	1.80±0.03	0.02±0.01
(P) ΔV_∞ mm/s	4.07	-5.26	13.45	-0.76	0.86	-4.56
(P) $\Delta\theta$ deg	1	1	2	4	5	-

The numerous EM anisotropy experiments discussed herein demonstrate that a dynamical 3-space exists and that the speed of the earth wrt this space exceeds 1 part in 1000 of c , namely a large effect. Not surprisingly this has indeed been detected many times over the last 125 years. The speed of ~ 500 km/s means that earth based clocks experience a real, so-called, time dilation effect from (3) of approximately 0.12s per day compared to cosmic time. However clocks may be corrected for this clock dilation effect because their speed v through space, which causes their slowing, is measurable by various experimental methods. This means that the absolute or cosmic time of the universe is measurable. This very much changes our understanding of time. However because of the inhomogeneity of the earth 3-space in-flow component the clock slowing effect causes a differential effect for clocks at different heights above the earth's surface. It was this effect that Pound and Rebka (1960) reported using the Harvard tower. Consider two clocks at heights h_1 and h_2 , with $h = h_2 - h_1$, then the frequency differential follows from Equation 34 to 38:

$$\frac{\Delta f}{f} = \sqrt{1 - \frac{v^2(h_2)}{c^2}} - \sqrt{1 - \frac{v^2(h_1)}{c^2}} \tag{34}$$

$$\approx \frac{v^2(h_1) - v^2(h_2)}{2c^2} + \dots \tag{35}$$

$$\frac{1}{2c^2} \frac{dv^2(r)}{dr} h + \dots \tag{36}$$

$$= \frac{g(r)h}{c^2} + \dots \tag{37}$$

$$= -\frac{\Delta\Phi}{c^2} + \dots \tag{38}$$

where, ϕ is the so-called 'gravitational potential' and with $v \cdot \nabla v = \nabla \left(\frac{v^2}{2} \right)$ for zero vorticity $\nabla \times v = 0$ and ignoring any time dependence of the flow and where finally, $\Delta\phi$ is the change in the gravitational potential. The actual process here is that, say, photons are emitted at the top of the tower with frequency f and reach the bottom detector with the same frequency f -there is no change in the frequency. This follows from (20) but with now $V = 0$ giving $T = T'$. However the bottom clock is running slower because the speed of space there is faster and so this clock determines that the falling photon has a

higher frequency, i.e., appears blue shifted. The opposite effect is seen for upward travelling photons, namely an apparent red shift as observed by the top clock. In practice the Pound-Rebka experiment used motion induced Doppler shifts to make these measurements using the Mossbauer effect. The overall conclusion is that Pound and Rebka measured the derivative of v^2 wrt height, whereas herein we have measured that actual speed, but averaged wrt the SC trajectory measurement protocol. It is important to note that the so-called "time dilation" effect is really a "clock slowing" effect-clocks are simply slowed by their movement through 3-space. The Gravity Probe A experiment also studied the clock slowing effect, though again interpreted differently therein and again complicated by additional Doppler effects.

The Cosmic Microwave Background (CMB) velocity is often confused with the Absolute Motion (AM) velocity or light-speed anisotropy velocity as determined in the experiments discussed herein. However these are unrelated and in fact point in very different directions, being almost at 90° to each other, with the CMB velocity being 369 km/s in direction ($\alpha = 11.2^\circ$, $\delta = -7.22^\circ$).

The CMB velocity is obtained by defining a frame of reference in which the thermalised CMB 3°K radiation is isotropic, that is by removing the dipole component and the CMB velocity is the velocity of the Earth in that frame. The CMB velocity is a measure of the motion of the solar system relative to the last scattering surface (a spherical shell) of the universe some 13.4 Gyrs in the past. The concept here is that at the time of decoupling of this radiation from matter that matter was on the whole, apart from small observable fluctuations, on average at rest with respect to the 3-space. So the CMB velocity is not motion with respect to the local 3-space now; that is the AM velocity. Contributions to the AM velocity would arise from the orbital motion of the solar system within the Milky Way galaxy, which has a speed of some 250 km s^{-1} and contributions from the motion of the Milky Way within the local cluster and so on to perhaps super clusters, as well as flows of space associated with gravity in the Milky Way and local galactic cluster. The difference between the CMB velocity and the AM velocity is explained by the spatial flows that are responsible for gravity at the galactic scales.

1.5. Optical Fiber Michelson Interferometers

The Michelson interferometer, having the calibration constant $k^2 = (n^2 - 1)(n^2 - 2)$ where n is the refractive index of the light-path medium, has zero sensitivity to EM anisotropy and gravitational waves when operated in vacuum-mode ($n = 1$). Fortunately the early experiments

had air present in the light paths (Michelson and Morley implicitly assumed that $k^2 = 1$, which considerably overestimated the sensitivity of their detector by a factor of ~1700 (air has $n = 1.00029$). This error led to the invention of “spacetime” in 1905. Miller avoided any assumptions about the sensitivity of his detector and used the earth orbit effect to estimate the calibration factor k^2 from his data, although even that is now known to be incorrect: The sun 3-space inflow component was unknown to Miller. It was only in 2002 that the design flaw in the Michelson interferometer was finally understood, (Cahill and Kitto, 2003). A very compact and cheap Michelson interferometric anisotropy and gravitational wave detector may be constructed using optical fibers (Cahill, 2007; Cahill and Stokes, 2008). But for most fibers $n \approx \sqrt{2}$ near room temperature, temperature and so needs to be operated at say 0°C. The (n^2-2) factor is caused by the Fresnel drag (Cahill and Brotherton, 2011). The schematic layout of the Michelson optical fiber interferometer is shown in **Fig. 12** and a photo shown in **Fig. 13**. Sample data is shown in **Fig. 14**. Two such detectors were operated in 2008 and some correlated waveforms were detected, (Cahill and Stokes, 2008).

The detection of light speed anisotropy-revealing a flow of space past the detector, is now entering an era of precision measurements, as reported herein. These are particularly important because experiments have shown

large turbulence effects in the flow and are beginning to characterise this turbulence. Such turbulence can be shown to correspond to what are, conventionally, known as gravitational waves, although not those implied by General Relativity, but more precisely are revealing a fractal structure to dynamical 3-space.

The detection and characterisation of these wave/turbulence effects requires only the development of small and cheap detectors, as these effects are large. However in all detectors the EM signals travel through a dielectric, either in bulk or optical fiber or through RF coaxial cables. For this reason it is important to understand the so-called Fresnel drag effect. In optical fibers the Fresnel drag effect has been established, as this is important in the operation of Sagnac optical fiber gyroscopes, for only then is the calibration independent of the fiber refractive index, as observed. The Fresnel drag effect is a phenomenological formalism that characterises the effect of the absolute motion of the propagation medium, say a dielectric, upon the speed of the EM radiation relative to that medium.

The Fresnel drag expression is that a dielectric in absolute motion through space at speed v , relative to space itself, causes the EM radiation to travel at speed Equation 39:

$$V(v) = \frac{c}{n} + v \left(1 - \frac{1}{n^2} \right) \tag{39}$$

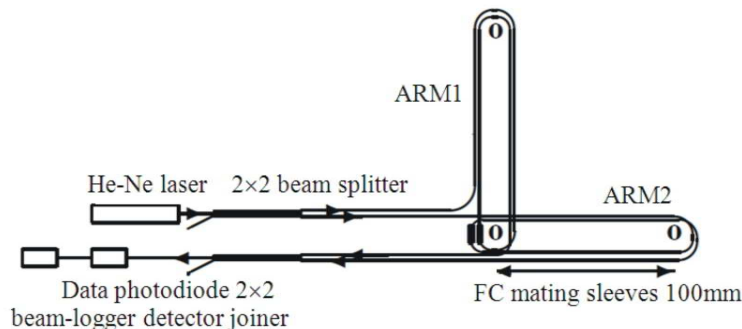


Fig. 12. Schematic layout of the interferometric optical-fiber light-speed anisotropy/gravitational wave detector. Actual detector is shown in **Fig. 13**. Coherent 633 nm light from the He-Ne Laser is split into two lengths of single-mode polarisation preserving fibers by the 2x2 beam splitter. The two fibers take different directions, ARM1 and ARM2, after which the light is recombined in the 2x2 beam joiner, in which the phase differences lead to interference effects that are indicated by the outgoing light intensity, which is measured in the photodiode detector/amplifier (Thorlabs PDA36A or PDA36A-EC) and then recorded in the data logger. In the actual layout the fibers make two loops in each arm, but with excess lengths wound around one arm (not shown) -to reduce effective fiber lengths so as to reduce sensitivity. The length of one straight section is 100 mm, which is the center to center spacing of the plastic turners, having diameter = 52mm, see **Fig. 13**. The relative travel times and hence the output light intensity, are affected by the varying speed and direction of the flowing 3-space, by affecting differentially the speed of the light and hence the net phase difference between the two arms. The detector was operated in fixed mode, with one arm NS and rotation achieved by rotation of the earth



Fig. 13. Photograph of an Optical Fiber Michelson Interferometer detector showing the optical fibers forming the two orthogonal arms. See **Fig. 12** for the schematic layout. The 2×2 beam splitter and joiner (Thorlabs FC632-50B-FC) are the two small stainless steel cylindrical tubes. The two FC to FC mating sleeves (Thorlabs ADAFC1) are physically adjacent. The overall dimensions of the metal base plate are 160mm×160mm. The 2×2 splitter and joiner each have two input and two output fibers, with one not used. Arm 2 is folded over the splitter and joiner, compared to the schematic layout. The interferometer shown costs approximately \$400

wrt the dielectric, when V and v have the same direction. Here n is the dielectric refractive index. The 2nd term is known as the Fresnel drag, appearing to show that the moving dielectric “drags” the EM radiation, although this is a misleading interpretation; see (Cahill and Brotherton, 2011), for a derivation (The Fresnel Drag in (39) can be “derived” from the Special Relativity velocity-addition formula, but there v is the speed of the dielectric wrt to the observer and as well common to both dielectrics and coaxial cables). If the Fresnel drag is always applicable then, as shown herein, a 1st order in v/c detector requires two clocks, though not necessarily synchronised, but requiring a rotation of the detector arm to extract the v -dependent term. However, as we show herein, if the Fresnel drag is not present in RF coaxial cables, then a detector 1st order in v/c and using one clock, can detect and characterise the dynamical space. In (Cahill and Brotherton, 2011) it was incorrectly concluded that the Fresnel effect was present in RF coaxial cables, for reasons related to the temperature effects.

In recent years there have been many vacuum-mode resonant cavity experiments with the aim of detecting light speed anisotropy, (Braximaier *et al.*, 2001; Lipa *et al.*, 2003; Muller *et al.*, 2003a; 2003b; Wolf *et al.*, 2003; 2004). However all these devices suffer from the same design flaw implicit in Michelson-type interferometers, namely zero sensitivity when operated in vacuum mode, because then the Lorentzian relativity physical arm contraction effect just happens to cancel the geometrical time difference effect. LIGO also has the same design flaw. However the proposed LISA space-based interferometer design does not suffer from this flaw, as there is no physical arm separating the “reflectors”-satellite based detectors. For this reason LISA will be excessively sensitive and may overload the data acquisition system. In any case the quantum zener diode detector technology has made all other techniques redundant.

1.6. Dual RF Coaxial Cable Detector

The Dual RF Coaxial Cable Detector (Cahill, 2012a) exploits the Fresnel drag anomaly, in that there is no Fresnel drag effect in RF coaxial cables, at low enough frequencies, **Fig. 15**.

Figure 16 shows the arrangement for measuring the one-way speed EM waves in RF coaxial cable. The actual travel time t_{AB} from A to B is determined by Equation 40:

$$V(v \cos(\theta))t_{AB} = L + v \cos(\theta)t_{AB} \quad (40)$$

where, the 2nd term comes from the end B moving an additional distance $v \cos(\theta)t_{AB}$ during time interval t_{AB} . Then Equation 41 and 42:

$$t_{AB} = \frac{L}{V(v \cos(\theta)) - v \cos(\theta)} = \frac{nL}{c} + \frac{v \cos(\theta)L}{c^2} \quad (41)$$

$$t_{CD} = \frac{L}{V(v \cos(\theta)) + v \cos(\theta)} = \frac{nL}{c} + \frac{v \cos(\theta)L}{c^2} \quad (42)$$

On using (39), i.e., assuming the validity of the Fresnel effect and expanding to 1st order in v/c . However if there is no Fresnel drag effect then we obtain Equation 43 and 44:

$$t_{AB} = \frac{L}{V(v \cos(\theta)) - v \cos(\theta)} = \frac{nL}{c} + \frac{v \cos(\theta)Ln^2}{c^2} \quad (43)$$

$$t_{CD} = \frac{L}{V(v \cos(\theta)) + v \cos(\theta)} = \frac{nL}{c} - \frac{v \cos(\theta)Ln^2}{c^2} \quad (44)$$

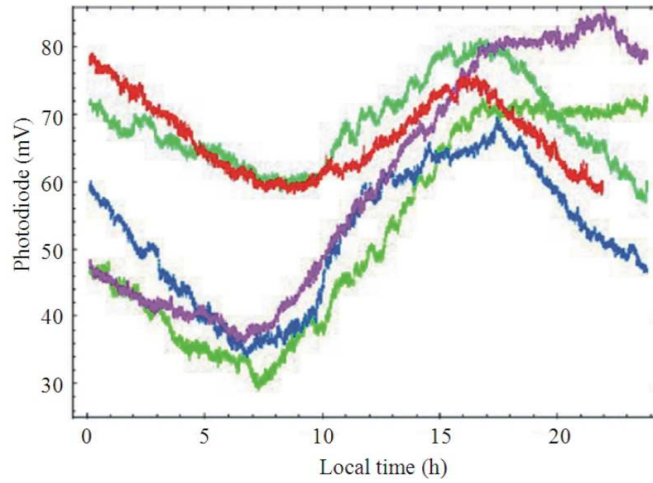


Fig. 14. D1 photodiode output voltage data (mV), recorded every 5 secs, from 5 successive days, starting September 22, 2007, plotted against local Adelaide time (UT = local time + 9.5 h). Local sidereal time \approx local time -15' for these days. Day sequence is indicated by increasing hue. Dominant minima and maxima is earth rotation effect. Fluctuations from day to day are evident as are fluctuations during each day - these are caused by wave effects in the flowing space. Changes in RA cause changes in timing of min/max, while changes in magnitude are caused by changes in declination and/or speed. So this data is consistent with the interferometer data in **Fig. 3**, as regards RA for maxima and minima, but with phase reversed. Two such detectors were operated in 2008 and some correlated waveforms were detected, (Cahill and Stokes, 2008). However there may be significant temperature effects in this data

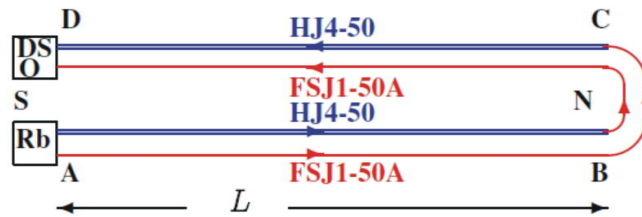


Fig. 15. Because Fresnel drag is absent in RF coaxial cables this dual cable setup, using one clock, is capable of detecting the absolute motion of the detector wrt to space, revealing the sidereal rotation effect as well as wave/turbulence effects. In the 1st trial of this detector this arrangement was used, with the cables laid out on a laboratory floor and results are shown in **Fig. 5**, bottom. In the new design the cables in each circuit are configured into 8 loops, as in **Fig. 17**, giving $L = 8 \times 1.85 \text{ m} = 14.8 \text{ m}$. In comparison with data from spacecraft earth-flyby Doppler shifts (Cahill, 2009c) this experiments confirms that there is no Fresnel drag effect in RF coaxial cables. In (Cahill, 2006a), a version with optical fibers in place of the HJ4-50 coaxial cables was used, see **Fig. 21**. There the optical fiber has a Fresnel drag effect while the coaxial cable did not. In that experiment optical-electrical converters were used to modulate/demodulate infrared light

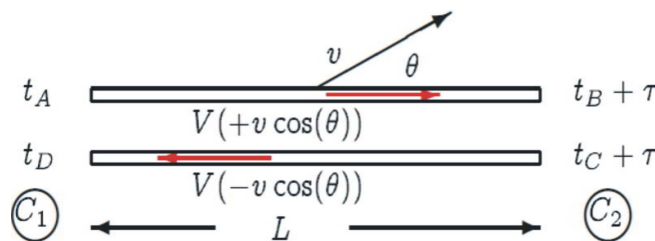


Fig. 16. Schematic layout for measuring the one-way speed of EM waves in RF coaxial cables, V is the speed of EM radiation wrt the apparatus, with or without the Fresnel drag, (39) and v is the speed of the apparatus through space, in direction v . Times here refer to absolute times

The important observation is that the v/c terms are independent of the dielectric refractive index n in (41) and (42), but have an n^2 dependence in (43) and (44), in the absence of the Fresnel drag effect. Then from (43) and (44) the round trip travel time is, **Fig. 15** Equation 45:

$$t_{AB} + t_{CD} = \frac{(n_1 + n_2)L}{c} + \frac{v \cos(\theta)L(n_1^2 - n_2^2)}{c^2} \quad (45)$$

where, n_1 and n_2 are the effective refractive indices for the two different RF coaxial cables, with two separate circuits to reduce temperature effects. Shown in **Fig. 17** is a photograph. The Andrews Phase Stabilised FSJ1-50A has $n_1 = 1.19$, while the HJ4-50 has $n_2 = 1.11$. One measures the travel time difference of two RF 10MHz signals from a Rubidium frequency standard (Rb) with a Digital Storage Oscilloscope (DSO). In each circuit the RF signal travels one-way in one type of coaxial cable and returns via a different kind of coaxial cable. Two circuits are used so that temperature effects cancel-if a temperature change alters the speed in one type of cable and so the travel time, that travel time change is the same in both circuits and cancels in the difference. The travel time difference of the two circuits at the DSO is Equation 46:

$$\Delta t = \frac{2v \cos(\theta)L(n_1^2 - n_2^2)}{c^2} \quad (46)$$

If the Fresnel drag effect occurred in RF coaxial cables, we would use (43) and (44) instead and then the $n_1^2 - n_2^2$ term is replaced by 0, i.e., there is no 1st order term in v .

The preliminary layout for this detector used cables laid out as in **Fig. 15** and the data is shown in **Fig. 5**. In the compact design the Andrew HJ4-50 cables are cut into 8×1.85 m shorter lengths in each circuit, corresponding to a net length of $L = 8 \times 1.85 = 14.8$ m and the Andrew FSJ1-50A cables are also cut, but into longer lengths to enable joining. However the curved parts of the Andrew FSJ1-50A cables contribute only at 2nd order in v/c . The apparatus was horizontal and orientated NS and used the rotation of the earth to change the angle θ . The dynamic range of $\cos(\theta)$, caused by the earth rotation only, is again $2 \sin(\lambda) \cos(\delta)$ where $\lambda = -35^\circ$ is the latitude of Adelaide. Inclining the detector at angle λ removes the earth rotation effect, as now the detector arm is parallel to the earth's spin axis, permitting a more accurate characterization of the wave effects.

The cable travel times and the DSO phase measurements still have a temperature dependence and these effects are removed from the data, rather than attempt to maintain a constant temperature, which is impractical because of the heat output of the Rb clock and

DSO. The detector was located in a closed room in which the temperature changed slowly over many days, with variations originating from changing external weather driven temperature changes. The temperature of the detector was measured and it was assumed that the timing errors were proportional to changes in that one measured temperature. These timing errors were some 30 ps, compared to the true signal of some 8ps. Because the temperature timing errors are much larger, the temperature induced $\Delta t = a + b\Delta T$ was fitted to the timing data and the coefficients a and b determined. Then this Δt time series was subtracted from the data, leaving the actual required phase data. This is particularly effective as the temperature variations had a distinctive time signature.

The phase data, after removing the temperature effects, is shown in **Fig. 18** (top), with the data compared with predictions for the sidereal effect only from the flyby Doppler shift data. As well that data is separated into two frequency bands (bottom), so that the sidereal effect is partially separated from the gravitational wave effect, viz 3-space wave turbulence. Being 1st order in v/c it is easily determined that the space flow is from the southerly direction. Miller (1933) reported the same sense, i.e., the flow is essentially from S to N, though using a 2nd order detector that is more difficult to determine. The frequency spectrum of this data is shown in **Fig. 19**, revealing a fractal $1/f$ form. This implies the fractal structure of the 3-space indicated in **Fig. 20**.

1.7. Optical Fiber Rf Coaxial Cable Detector

An earlier 1st order in v/c gravitational wave detector design is shown in **Fig. 21**, with some data shown in **Fig. 22**. Only now is it known why that detector also worked, namely that there is a Fresnel drag effect in the optical fibers, but not in the RF coaxial cable. Then the travel time difference, measured at the DSO, is given by Equation 47:

$$\Delta t = \frac{2v \cos(\theta)L(n_1^2 - 1)}{c^2} \quad (47)$$

where, n_1 is the effective refractive index of the RF coaxial cable. Again the data is in remarkable agreement with the flyby and other detections of v .

The Dual RF Coaxial Cable Detector exploits the Fresnel drag anomaly in RF coaxial cables, viz the drag effect is absent in such cables, for reasons unknown and this 1st order in v/c detector is compact, robust and uses one clock. This anomaly now explains the operation of the Optical-Fiber-Coaxial Cable Detector and permits a new calibration. These detectors have confirmed the absolute motion of the solar system and the gravitational wave effects seen in the earlier experiments of Michelson-Morley, Miller, DeWitte.

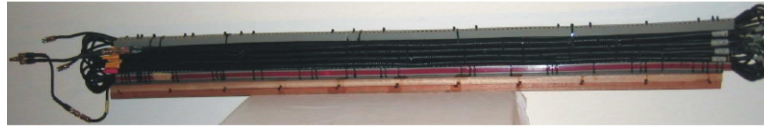


Fig. 17. Photograph of the RF coaxial cables arrangement, based upon 16×1.85m lengths of phase stabilised Andrew HJ4-50 coaxial cable. These are joined to 16 lengths of phase stabilised Andrew FSJ1-50A cable, in the manner shown schematically in **Fig.15**. The 16 HJ4-50 coaxial cables have been tightly bound into a 4×4 array, so that the cables, locally, have the same temperature, with cables in one of the circuits embedded between cables in the 2nd circuit. This arrangement of the cables permits the cancellation of temperature differential effects in the cables. A similar array of the smaller diameter FSJ1-50A cables is located inside the grey-coloured conduit boxes

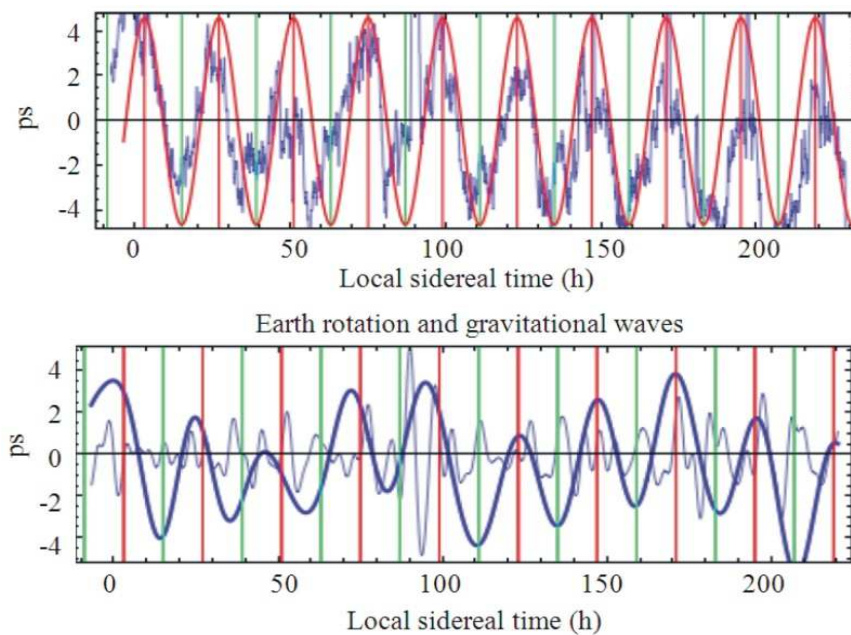


Fig. 18. Top: Travel time differences (ps) between the two coaxial cable circuits in **Fig. 15**, orientated NS and horizontal, over 9 days (March 4-12, 2012, Adelaide) plotted against local sidereal time. Sinewave, with dynamic range 8.03 ps, is prediction for sidereal effect from flyby Doppler shift data for RA = 2.75 h (shown by red fiducial lines), Dec. = -76.6° and with speed 499.2 km/s, see **Table 1**. Data shows sidereal effect and significant wave/turbulence effects. Bottom: Data filtered into two frequency bands $3.4 \times 10^{-3} \text{ MHz} < f < 0.018 \text{ MHz}$ ($81.4 \text{ h} > T > 15.3 \text{ h}$) and $0.018 \text{ MHz} < f < 0.067 \text{ MHz}$ ($15.3 \text{ h} > T > 4.14 \text{ h}$), showing more clearly the earth rotation sidereal effect (plus vlf waves) and the turbulence without the sidereal effect. Frequency spectrum of top data is shown in **Fig. 19**

Most significantly these experiments agree with one another and with the absolute motion velocity vector determined from spacecraft earth-flyby Doppler shifts. The observed significant wave/turbulence effects reveal that the so-called “gravitational waves” are easily detectable in small-scale laboratory detectors and are considerably larger than those predicted by GR. These effects are not detectable in vacuum-mode Michelson terrestrial interferometers, nor by their analogue vacuum-mode resonant cavity experiments.

The Dual RF Coaxial Cable Detector permits a detailed study and characterisation of the wave effects and with the detector having the inclination equal to the local latitude the earth rotation effect may be removed, as the detector is then parallel to the earth’s spin axis, enabling a more accurate characterisation of the wave effects. The major discovery arising from these various results is that 3-space is directly detectable and has a fractal textured structure. This and numerous other effects are consistent with the

dynamical theory for this 3-space. We are seeing the emergence of fundamentally new physics, with space being a non-geometrical dynamical system and fractal

down to the smallest scales describable by a classical velocity field and below that by quantum foam dynamics (Cahill, 2005a).

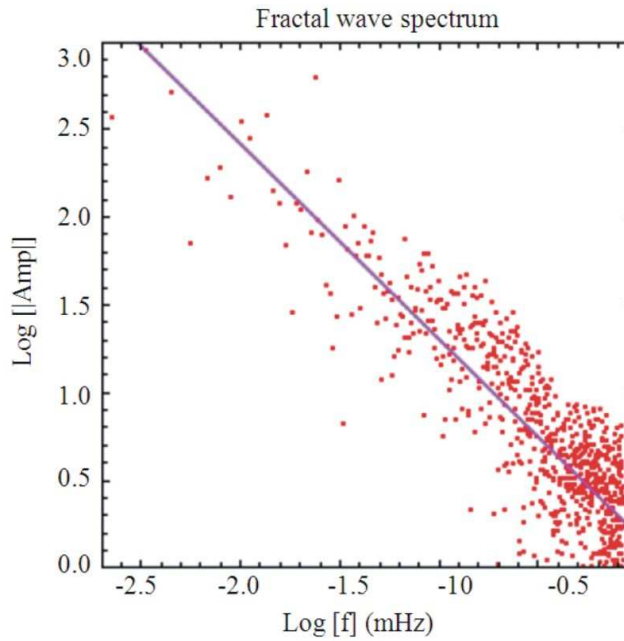


Fig. 19. Log-Log plot of the data (top) in Fig.18, with the straight line being $A/f = 1$, indicating a $1=f$ fractal wave spectrum. The interpretation for this is the 3-space structure shown in Fig. 20

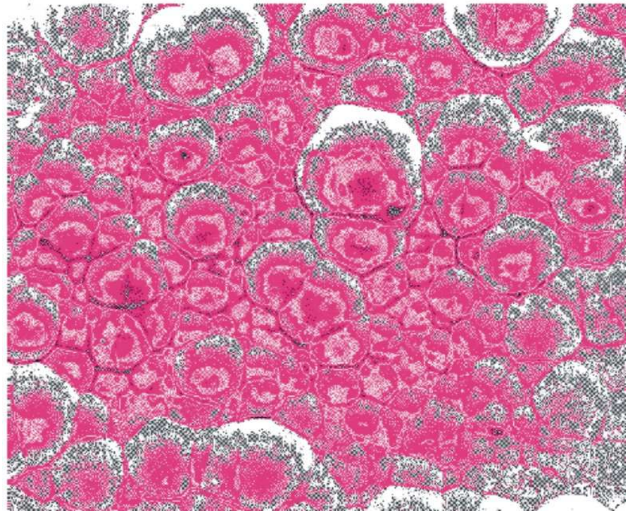


Fig. 20. Representation of the fractal wave data as a revealing the fractal textured structure of the 3-space, with cells of space having slightly different velocities and continually changing and moving wrt the earth with a speed of $\sim 500 \text{ km s}^{-1}$

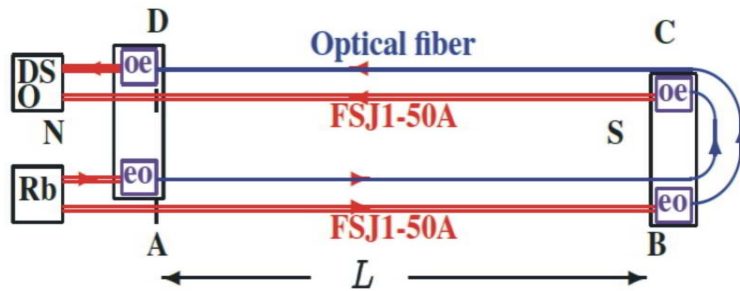


Fig. 21. Layout of the optical fiber-coaxial cable detector, with $L = 5.0$ m. 10 MHz RF signals come from the Rubidium atomic clock (Rb). The Electrical to Optical converters (EO) use the RF signals to modulate $1.3 \mu\text{m}$ infrared signals that propagate through the single-mode optical fibers. The Optical to Electrical converters (OE) demodulate that signal and give the two RF signals that finally reach the Digital Storage Oscilloscope (DSO), which measures their phase difference. The key effects are that the propagation speeds through the coaxial cables and optical fibers respond differently to their absolute motion through space, with no Fresnel drag in the coaxial cables and Fresnel drag effect in the optical fibers. Without this key difference this detector does not work

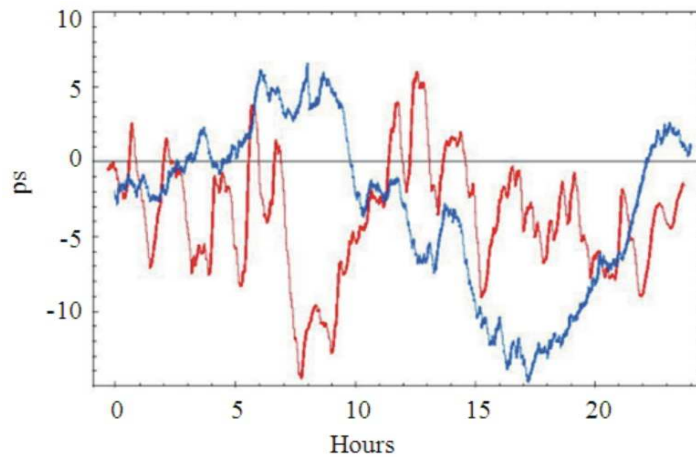


Fig.22. Phase difference (ps), with arbitrary zero, versus local time data plots from the Optical Fiber-Coaxial Cable Detector, **Fig. 21** and (Cahill, 2006a; 2006b), showing the sidereal time effect and significant wave/turbulence effects. The plot (blue) with the most easily identified minimum at ~ 17 h local Adelaide time is from June 9, 2006, while the plot (red) with the minimum at ~ 8.5 h local time is from August 23, 2006. We see that the minimum has moved forward in time by approximately 8.5 h. The expected sidereal shift for this 65 day difference, without wave effects, is 4.3 h, to which must be added another ~ 1 h from the aberration effects shown in **Fig. 11**, giving 5.3 h, in agreement with the data, considering that on individual days the min/max fluctuates by ± 2 h. This sidereal time shift is a critical test for the detector. From the flyby Doppler data we have for August RA = 5 h, Dec. = -70° and speed 478 km s^{-1} , see **Table 1**, giving a predicted sidereal effect dynamic range to be 8.6 ps, very close to that observed

1.8. Quantum Zener Diode Detectors

When extending the Dual RF Coaxial Cable Detector experiment to include one located in London, in addition to that located in Adelaide, an analysis of the measured DSO internal noise in each identically setup instrument was undertaken, when the extensive RF coaxial cable array was replaced by short leads.

This was intended to determine the S/N ratio for the joint Adelaide-London experiment. Surprisingly the internal noise was found to be correlated, with the noise in the London DSO being some 13 to 20 sec behind the Adelaide DSO (LeCroy WaveRunner 6051A DSOs were used) noise, **Fig. 23**. The correlation data had a phase that tracked sidereal time, meaning that the average direction was approximately

fixed wrt the galaxy, but with extensive fluctuations as well from the gravitational wave/turbulence effect, that had been seen in all previous experiments. The explanation for this DSO effect was not possible as the DSO is a complex instruments and which component was responding to the passing space fluctuations could not be determined. But the correlation analysis did demonstrate that not all of the internal noise in the DSO was being caused solely by some random process intrinsic to the instrument. Subsequent experiments, below, now suggest that there are zener diodes within the time difference measurements hardware within the DSO.

The travel time delay $\tau(t)$ was determined by computing the correlation function Equation 48:

$$C(\tau, t) = \int_{t-T}^{t+T} dt' S_1(t' - \tau/2) S_2[t' + \tau/2] e^{-a(t'-t)^2} \quad (48)$$

For the two detector signals $S_1(t)$ and $S_2(t)$. Here $2T = 200s$ is the time interval used, about UTC time t . The gaussian term ensures the absence of end-effects. Maximising $C(\tau, t)$ wrt τ gives $\tau(t)$ -the delay time vs UTCt and plotted in **Fig. 24 and 25**, where the data has been binned into 1h time intervals and the rms also shown. The speed and direction, over a 24h period, was determined by fitting the time delay data using Equation 49:

$$\tau = \frac{R.v}{v^2} \quad (49)$$

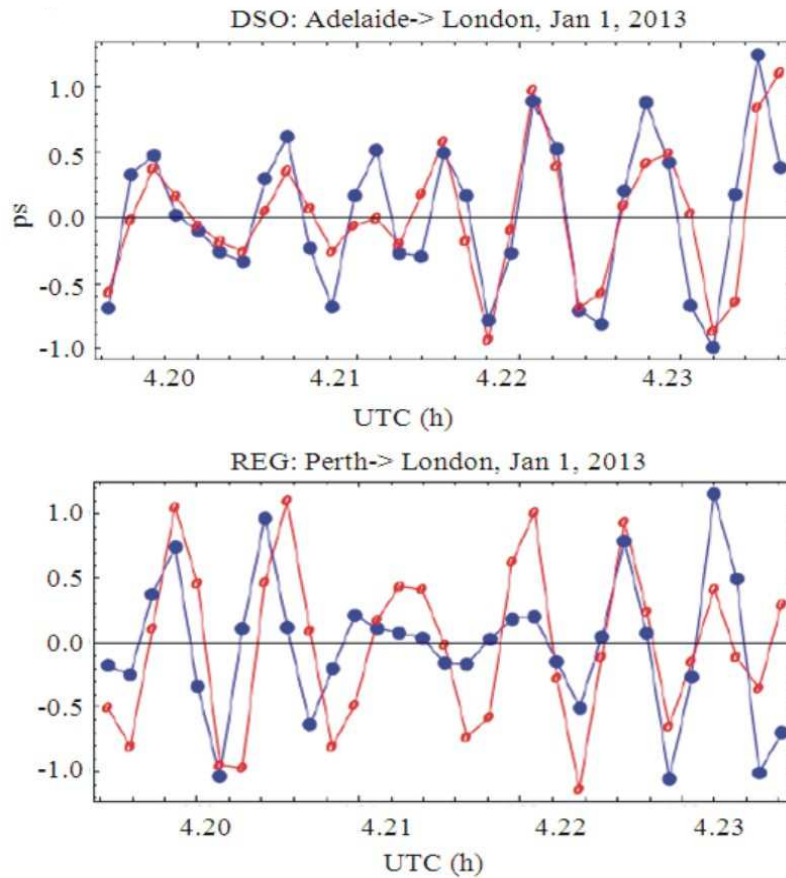


Fig. 23. Correlations in band-passed Adelaide-London DSO data (top) and Perth (Australia)-London REG data (bottom), for January 1, 2013, with London data (red, open dots) advanced by 15s in both cases, over the same 200s time interval. The data points are at 5s intervals. The REG data was recorded every 1s and has been averaged to 5s intervals for ease of comparison with DSO data. The data shows a quasi-periodicity of ~20s, related to the reverberation effect (Cahill and Deane, 2013). The UTC time at all detectors was determined using internet timing applications, which have ms precision

where, R is the Adelaide-London spatial separation vector and $v(\theta, \delta)$ is the 3-space velocity vector, parametrised by a speed, RA and Declination. This expression assumes a plane wave form for the gravitational waves. The $\tau(t)$ delay times show large fluctuations, corresponding to fluctuations in speed and/or direction, as also seen in the data in **Fig. 3** and also a quasi-periodicity, as seen in **Fig. 23**. Then only minimal travel times, $10s < \tau < 22s$, were retained. Correlations, as shown in **Fig. 23**, are not always evident and then the correlation function $C(\tau, t)$ has a low value. Only $\tau(t)$ data from high values of the correlation function were used. The absence of correlations at all times is expected as the London detector is not directly “downstream” of the Adelaide detector and so a fractal structure to space, possessing a spatial inhomogeneity, bars ongoing correlations and as well the wave structure will evolve during the travel time. **Figure 23** shows examples of significant correlations in phase and amplitude between all four detectors, but with some mismatches. The approximate travel time of 15s in **Fig. 23** at ~ 4.2 h UTC is also apparent in **Fig. 24**, with the top figure showing the discovery of the correlations from the two DSO separated by a distance $R \approx 12160$ km. That the internal “noise” in these DSO is correlated is a major discovery.

There are much simpler devices that were discovered to also display time delayed correlations over large distances: These are the Random Number Generators (RNG) or Random Event Generators (REG). There are various designs available from manufacturers and all claim that these devices manifest hardware random quantum processes, as they involve the quantum to classical transition when a measurements, say, of the quantum tunnelling of electrons through a nanotechnology potential barrier, ~ 10 nm thickness, is measured by a classical/macroscopic system. According to the standard interpretation of the quantum theory, the collapse of the electron wave function to one side or the other of the barrier, after the tunnelling produces a component on each side, is purely a random event, internal to the quantum system. However this interpretation had never been tested experimentally. Guided by the results from the DSO correlated-noise effect, the data from two REGs, located in Perth and London, was examined. The data (The data is from the GCP international network: <http://teihard.globalmind.org/>) showed the same correlation effect as observed in the DSO experiments, **Fig. 23-25**. However REGs typically employ a XOR gate that produces integer valued outputs with a predetermined statistical form.

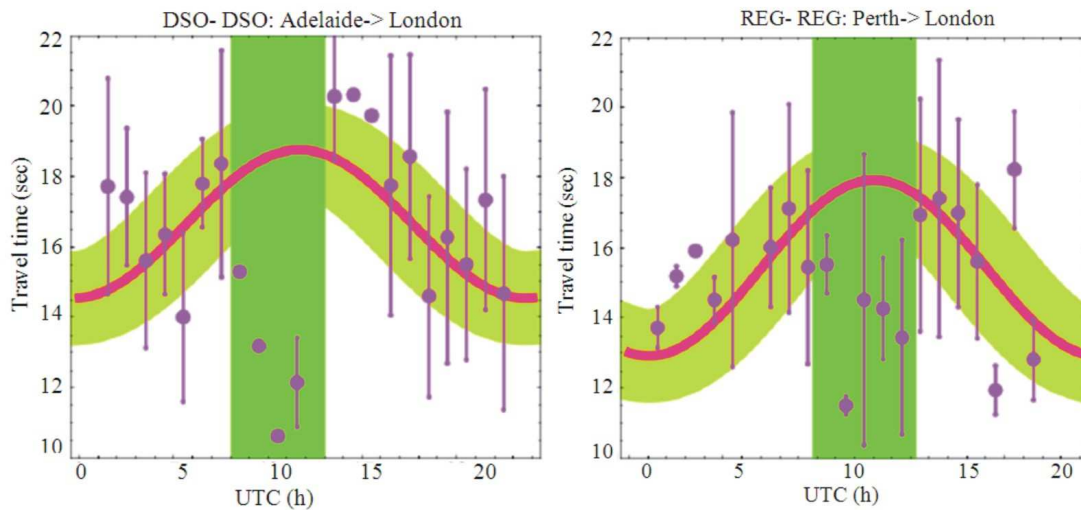


Fig. 24. Travel times from DSO-DSO Adelaide-London data (top) and REG-REG Perth-London data (bottom) from correlation analysis using (48). The data in each 1 h interval has been binned and the average and rms shown. The thick (red line) shows best fit to data using plane wave travel time predictor, (49), but after excluding those data points between 8 and 13 h UTC (top) and 10 and 15 h UTC (bottom), indicated by vertical band. Those data points are not consistent with the plane wave modelling and suggest a scattering process when the waves pass deeper into the earth, **Fig. 26**. The Perth-London phase is retarded wrt Adelaide-London phase by ~ 1.5 h, consistent with Perth being 1.5h west of Adelaide. The Adelaide-London data gives speed = 512 km s^{-1} , RA = 4.8 h, Dec. = 83°S and the Perth-London data gives speed = 528 km s^{-1} , RA = 5.3 h, Dec. = 81°S . The broad band tracking the best fit line is for ± 1 sec fluctuations, corresponding to speed fluctuation of $\pm 17 \text{ km s}^{-1}$. Actual fluctuations are larger than this, as 1st observed by Michelson-Morley and by Miller, **Fig. 3**

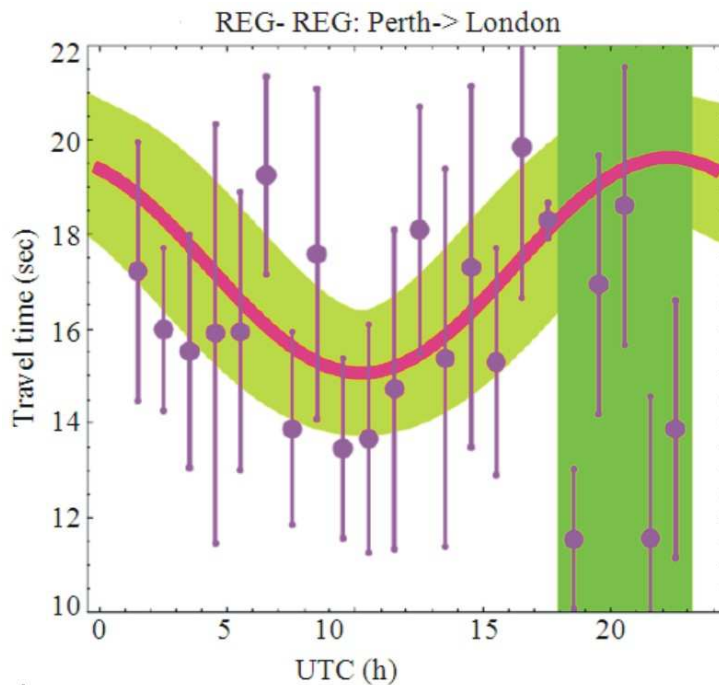


Fig. 25. Travel times from REG-REG Perth-London data for August 1, 2012. The data in each 1 h interval has been binned and the average and rms shown. The thick (red line) shows best fit to data using plane wave travel time predictor, (49), but after excluding those data points between 18 and 23 h UTC, indicated by vertical band. Those data points are not consistent with the plane wave modelling. This data gives speed = 471 km s^{-1} , RA = 4.4 h, Dec. = 82°S . The change in phase of the maximum of the data, from UTC= 22 ± 2 h, for August 1, 2012, to UTC = 12 ± 2 h for January 2013 (**Fig. 24**), but with essentially the same RA, illustrates the sidereal effect: The average direction of the space flow is fixed wrt to the stars, apart from the earth-orbit aberration effect, **Fig. 11**

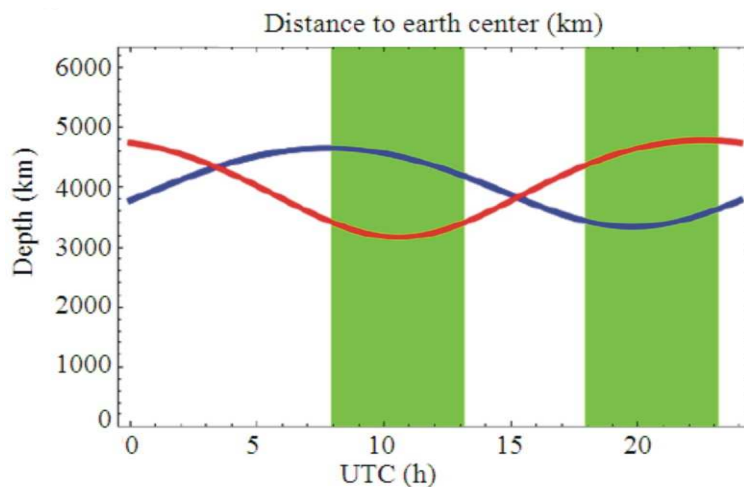


Fig. 26. Given measured space velocity, plots show maximum earth penetration depth of space detected by London detectors for Adelaide→London, Jan. 1, 2013 (red) and Perth→London, August 1, 2012 (blue), revealing that the anomalous scattering occurs when deeper depths are “traversed”. The vertical shadings correspond to those in **Fig. 24** (top) and **Fig. 25**

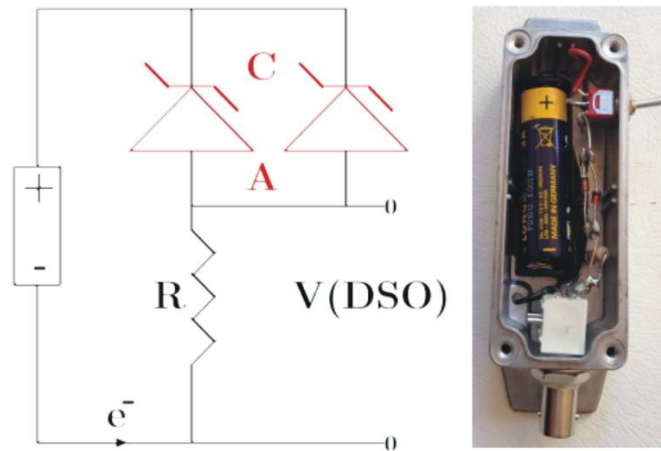


Fig. 27. Left: Circuit of Zener Diode GravitationalWave Detector, showing 1.5V AA battery, two 1N4728A zener diodes operating in reverse bias mode and having a Zener voltage of 3.3V and resistor $R = 10\text{ K}\Omega$. Voltage V across resistor is measured and used to determine the space driven fluctuating tunnelling current through the zener diodes. Correlated currents from two collocated detectors are shown in **Fig. 28**. Right: Photo of detector with 5 zener diodes in parallel

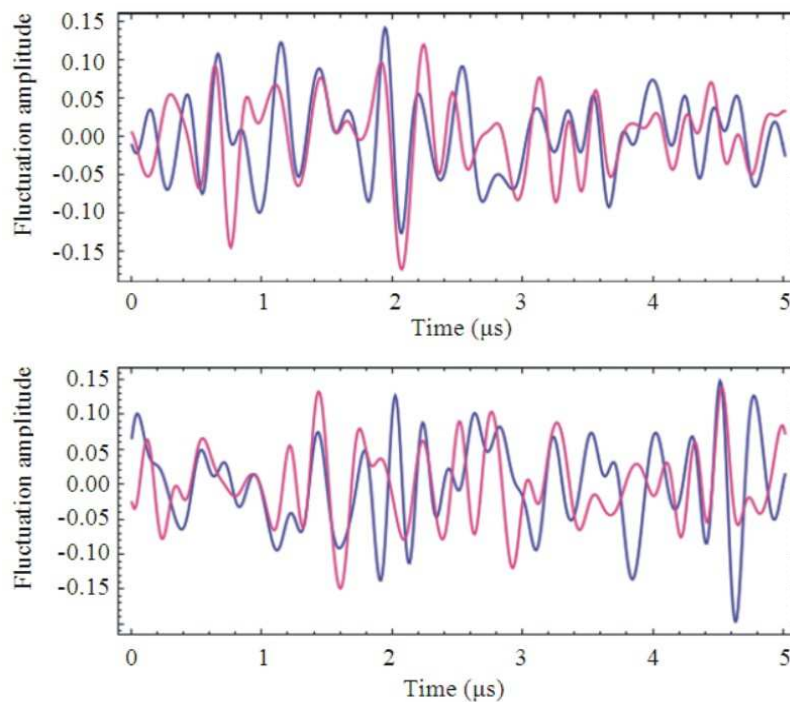


Fig. 28. Top: Current fluctuations from two collocated zener diode detectors, **Fig. 27** (separated by 3-4 cm in EW direction due to box size), revealing strong correlations. The small separation may explain slight differences, revealing a structure to space at very small distance scales. Bottom: Correlations when detectors separated NS by approximately 25 cm and with N detector signal advanced by $0.5\ \mu\text{s}$ and then showing strong correlations. This time delay effect reveals space traveling from S to N at a speed of approximately 500 km s^{-1} . **Figure 29** shows plot of correlation function $C(\tau, t)$ with time delay τ expressed as a speed over a distance of 25 cm

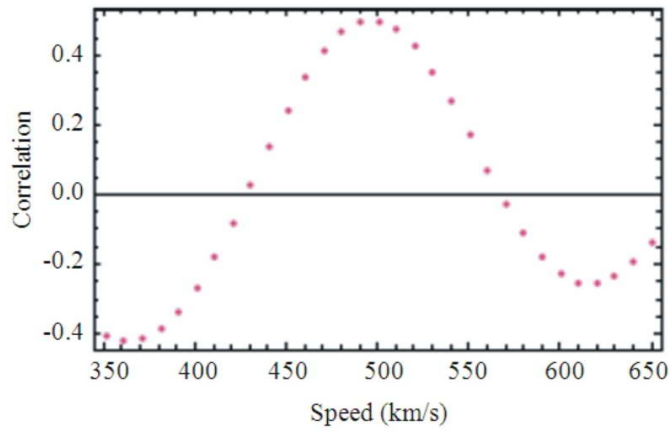


Fig. 29. Correlation function $C(\tau, t)$, (48), with time delay τ expressed as a speed over a distance of 25 cm, for the data shown in **Fig. 28**, Bottom. t is the time of observation, which is not relevant in this test case. This plot reveals a speed of $500 \pm 25 \text{ km s}^{-1}$

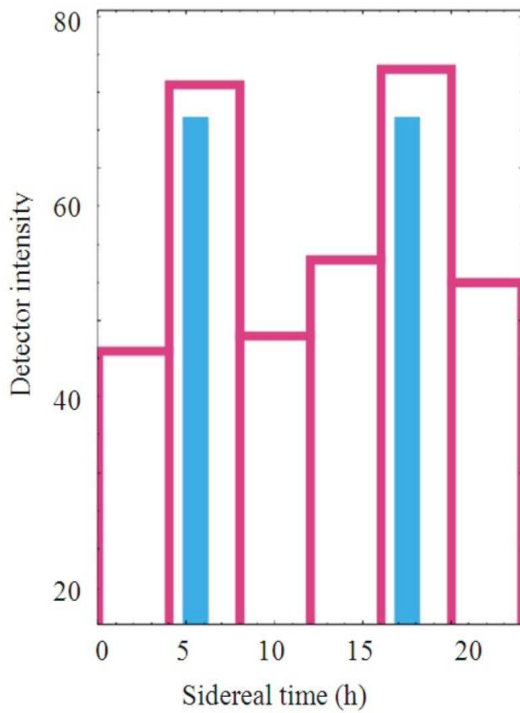


Fig. 30. Weber 24h histogram of detector intensity (the number of coincidences in each bin) versus sidereal time, adapted from (Weber, 1969; 1970; 1972). Vertical lines at 5.5 h and 17.5 h are RA for 3-space flow 1st determined by Miller using a gas-mode Michelson interferometer in 1925/26. The width of these lines is an indication of the variability of the RA over a year caused by the earth orbit aberration effect. The explanation for the maxima in coincidences at these sidereal times is explained in the **Fig. 32**

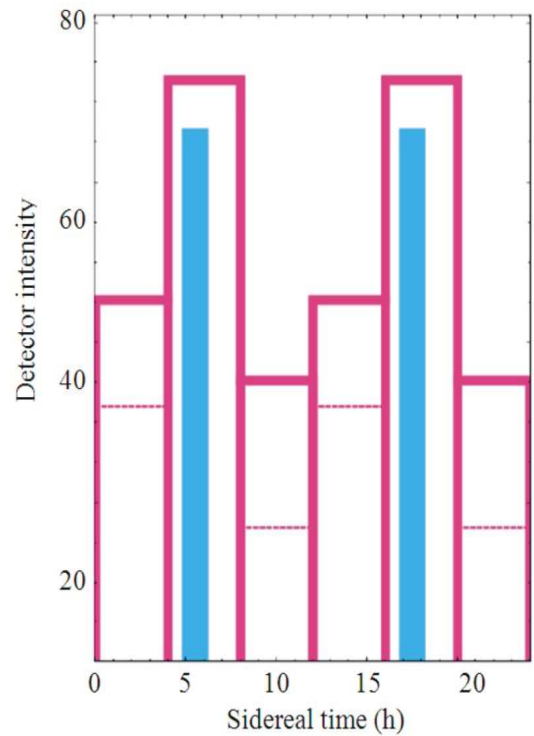


Fig. 31. Predicted histogram of detector intensity (the number of coincidences in each bin) versus sidereal time, from binning the predicted double-hump form in **Fig. 32**. Here a constant background is added. Without that background the lower valued histogram bars are shown dashed. The scale is arbitrary, as the detector sensitivity to 3-space velocity fluctuations is unknown. This predicted form is to be compared with Weber's actual data, **Fig. 30**

To study the zener diode tunnelling currents without XOR gate intervention two collocated zener diode circuits were used to detect highly correlated tunnelling currents, **Fig. 27 and 28**. When the detectors are separated by ~ 0.25 m in NS direction, phase differences $\sim 0.5 \mu\text{s}$ were observed and dependent on relative orientation. So this zener diode circuit forms a very simple and cheap nanotechnology quantum detector for gravitational waves.

1.9. Weber Resonant Bar Detectors

Weber (1969) reported the 1st coincidence data from two dedicated gravitational wave resonant bar detectors located in Argonne and Maryland and reported the coincidences shown in **Fig. 30**. These results were criticised on a number of spurious grounds, all being along the lines that the data was inconsistent with the predictions of GR, which indeed it is, see (Collins, 2004). This experiment was followed by other similar experiments, none of which reported similar effects. **Figure 31** shows the predicted data using the known speed and direction of the 3-space velocity, measured in numerous other experiments discussed herein and using a assumptions outlined in **Fig. 32**. Given these assumptions the Weber data looks remarkably similar to the predicted form.

1.10. Amaldi Resonant Bar Detectors

On the basis of data from the new nanotechnology zener diode quantum gravitational wave detectors (Cahill, 2013b) it is argued that the wave effects detected by (Amaldi *et al.*, 1981a; 1981b), using two cryogenic bar detectors, located in Frascati and Rome, were genuine gravitational wave effects, together with earth oscillation effects, although not gravitational waves of the expected form.

The speed and direction of gravitational waves have been repeatedly detected using a variety of techniques over the last 125 years and have a speed of some 500 km s^{-1} coming from a direction with RA $\sim 5\text{h}$, Dec. $\sim 80^\circ$. These waves appear to be of galactic origin and associated with the dynamics of the galaxy and perhaps the local cluster. This speed is that of the dynamical 3-space, which appears to have a fractal structure and the significant magnitude waves are turbulence/fractal structure in that flowing space. The detection techniques include gas-mode Michelson interferometers, RF coaxial cable EM speed measurements, RF coaxial-cable-optical fiber RF/EM speed measurements, EM speed measurements from spacecraft Earth-flyby Doppler shifts, zenerdiode quantum detectors, within Digital Storage

Oscilloscopes and in so-called Random Event Generators (REG); (Cahill, 2009c; 2012a; 2013b). These zener diode devices have detected correlations between Adelaide and London and between Perth and London, with travel time delays from 10 to 20 sec and with significant reverberation effects (Cahill and Deane, 2013). The zener diode gravitational wave quantum detectors operate by the process of the 3-space wave turbulence causing the quantum to classical transition, i.e., spatial localisation, of the electron wave functions tunneling through a 10 nm quantum barrier, when the diode is operated in reverse bias. The earlier techniques rely on detecting EM radiation anisotropy.

Data was collected with two cryogenic resonant gravitational wave antennas operated simultaneously in Rome and Frascati. Coincidences were detected with pulses lasting about 1 se and travel times differing from one second to twenty seconds ($\pm 0.5\text{s}$), with the NW Rome signal delayed relative to the Frascati events. These events were dismissed as gravitational wave events as the travel times, for the 20 km separation, far exceed that expected if one assumes that gravitational waves travel at speed c , predicting travel times $\sim 0.1 \text{ ms}$. As well frequency analysis of the data revealed strong peaks at frequencies coinciding with known vibration frequencies of the earth, see bottom plot of **Fig. 34**. Amaldi *et al.* (1981a) considered several mechanisms for the detection of such frequencies: (i) various instrumental couplings to the earth vibrations, (ii) gravitational field variations caused by a terrestrial source. However the very same results are obtained with the zener diode quantum gravitational wave detectors.

The zener diode detectors first used are known as Random Number Generators (RNG) or Random Event Generators (REG). There are various designs available from manufacturers and all claim that these devices manifest hardware random quantum processes, as they involve the quantum to classical transition when a measurements, say, of the quantum tunnelling of electrons through a nanotechnology potential barrier, $\sim 10 \text{ nm}$ thickness, is measured by a classical/macroscopic system. According to the standard interpretation of the quantum theory, the collapse of the electron wave function to one side or the other of the barrier, after the tunnelling produces a component on each side, is purely a random event, internal to the quantum system. However that interpretation had never been tested experimentally, until (Cahill, 2013b). Data from two REGs, located in Perth and London, was examined. The above mentioned travel times were then

observed. The key features being a speed of $\sim 500 \text{ km s}^{-1}$ and strong reverberation effects, see **Fig. 33**.

Using data from REG's located in Perth and London, for Jan.1-3, 2013 and then doing a Fourier transform frequency analysis, we obtain the spectrum in the top two plots in **Fig. 34**. The unfiltered power spectra from

the two REGs show remarkable similarity to each other and to the spectrum from the Frascati data. Again the dominant frequencies correspond to known earth vibration frequencies (Masters and Widmer, 1985) although there are long-period oscillations, common to all detectors that are not known earth frequencies.

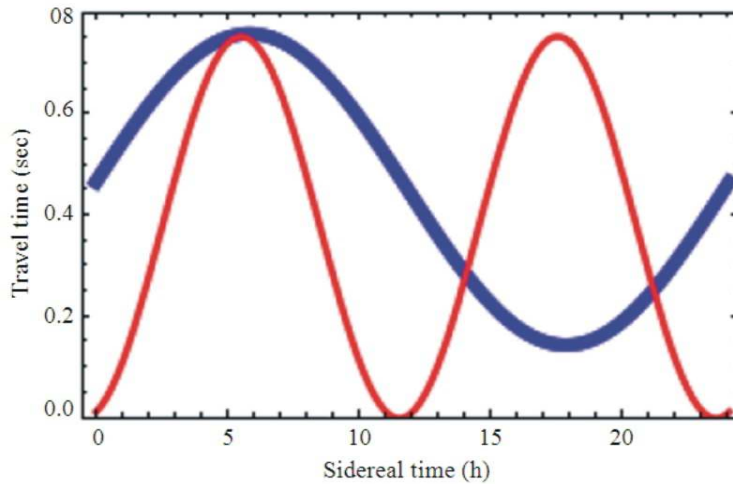


Fig. 32. The blue single-hump plot shows predicted delay time, sec, for the two Weber detectors, for projected waves from Maryland (39° N , $76^\circ 56' \text{ W}$) to Argonne ($41^\circ 43' \text{ N}$, $87^\circ 100' \text{ W}$), a distance of 914 km, for a 3-space velocity of 500 km s^{-1} from the direction $\text{RA} = 5.5\text{h}$, $\text{Dec.} = 80^\circ \text{S}$. The resonant bar detectors were orientated EW. It is assumed that they would be excited most easily by 3-space velocity fluctuations in the EW direction. The red double-humped plot shows the 3-space velocity projected onto the EW direction and squared (scale is arbitrary), this being taken as a measure of the excitation of the detector. Binning that plot gives **Fig. 31**, which is very similar to Weber's actual data, **Fig. 30**

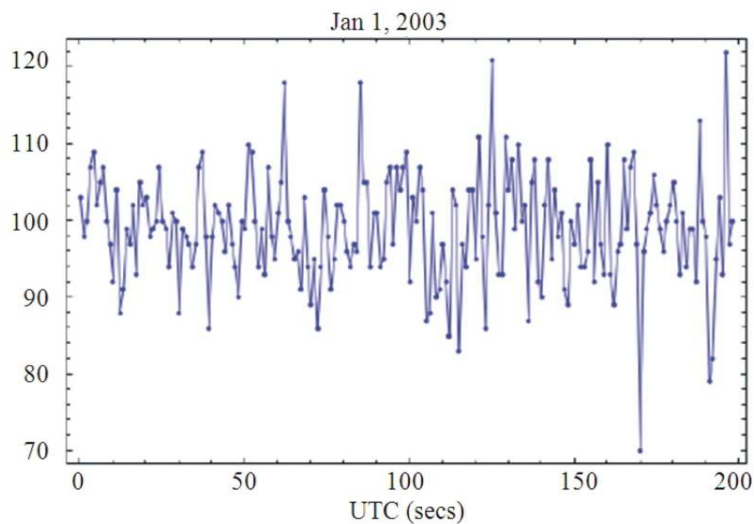


Fig. 33. Perth zener diode quantum detector (REG) data, for January 1, 2013. The data points are at 1s intervals. The data shows strong peaks at 5-30s intervals, related to the reverberation effect (Cahill and Deane, 2013). This appears to be the time-delay effect detected between the Frascati and Rome cryogenic gravitational wave bar detectors (Amaldi, 1981a; 1981b)

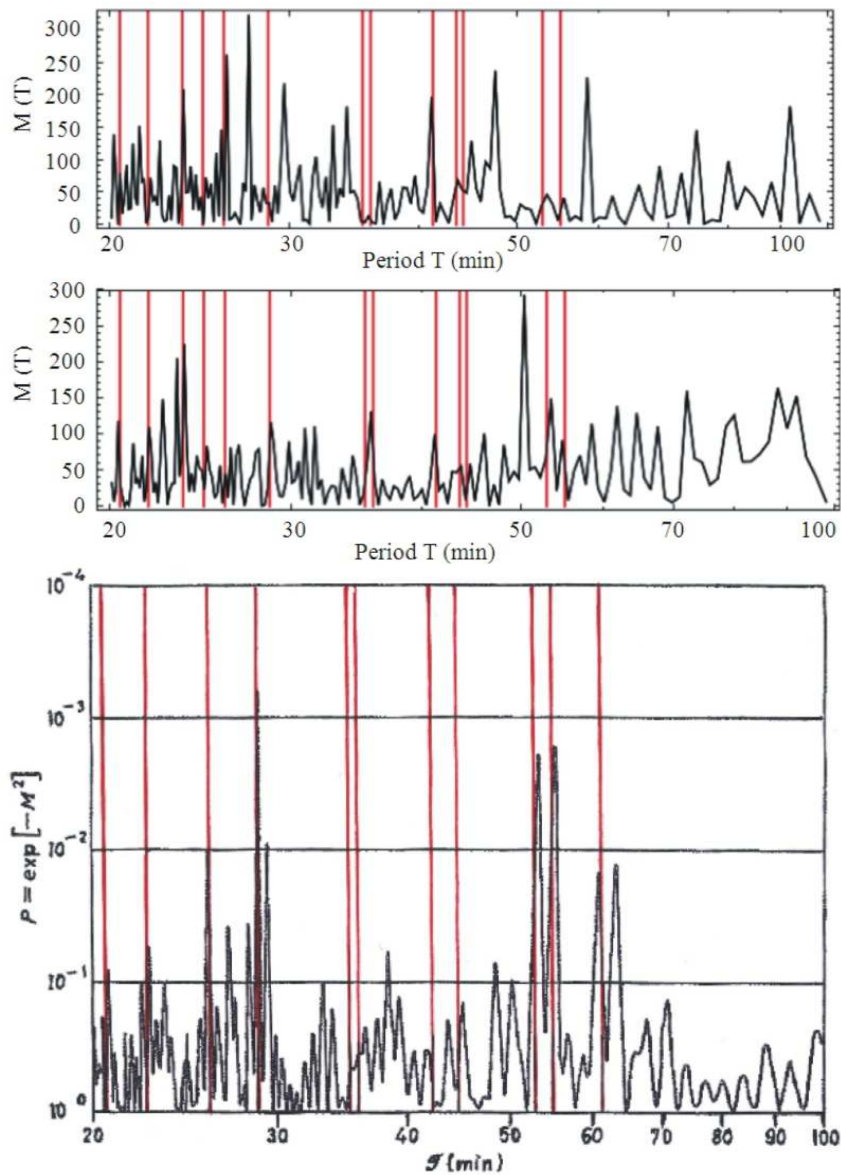


Fig. 34. Top: Power spectrum from Zener Diode detector in Perth, Jan 1-3, 2013. Middle: Power spectrum from Zener Diode detector in London, Jan 1-3, 2013. Bottom: Power spectrum from Frascati bar detector data, May 6-7, 1980, adapted from (Amaldi 1981a; 1981b). Vertical lines (red) show various earth vibration periods, determined by seismology, (Masters and Widmer, 1985). $M(T) = |F(T)|^2$ is the power spectrum, expressed as a function of period T , where $F(T)$ is the Fourier transform of the data time series. A 200 sec interval of the Perth data is shown in **Fig. 33**. The spectra from all detectors show the same low frequency peaks, but with differing intensities. The peaks at 53.1 and 54.1 min equal the ${}_0S_2^{+1}$ and ${}_0S_2^{-1}$ Earth vibration modes

This new data shows that the time delays observed between Frascati and Rome are to be expected, because of the strong reverberation effects seen in the zener diode detector data. However the occurrence of the earth

vibration frequencies is intriguing and reveals new physics. Unlike the bar detectors it is impossible for any physical earth movement to mechanically affect the zener diodes and so all detectors are responding to

dynamical space fluctuations caused by the oscillations of the matter forming the earth. The key questions is what causes this ongoing activation of the earth modes? Are they caused by earthquakes or by the fractal 3-space waves exciting the earth modes?

1.11. Dynamical 3-Space

If Michelson and Morley had more carefully presented their pioneering data physics would have developed in a very different direction. Even by 1925/26 Miller, a junior colleague of Michelson, was repeating the gas-mode interferometer experiment and by not using Newtonian mechanics to attempt a calibration of the device, rather by using the earth aberration effect which utilised the earth orbital speed of 30 km s^{-1} to set the calibration constant, although that also entailed false assumptions. The experimental data reveals the existence of a dynamical space. It is a simple matter to derive the dynamics of space and the emergence of gravity as a quantum matter effect.

Physics must employ a covariance formulation, in the sense that ultimately predictions are independent of observers and that there must also be a relativity principle that relates observational data by different observers. We assume then that space has a structure whose movement, wrt an observer, is described by a velocity field, $v(r; t)$, at the classical physics level, at a location r and time t , as defined by the observer. In particular the space coordinates r define an embedding space, which herein we take to be Euclidean. At a deeper level space is probably a fractal quantum foam, which is only approximately embeddable in a 3-dimensional space at a coarsegrained level, (Cahill, 2005a; 2009b; 2011a). This embedding space has no ontological existence- it is not real. Ironically Newton took this space to be real but unobservable and so a different concept and so excluding the possibility that gravity was caused by an accelerating space. It is assumed that different observers, in relative uniform motion, relate their description of the velocity field by means of the Galilean Relativity Transformation for positions and velocities. It is usually argued that the Galilean Relativity Transformations were made redundant and in error by the Special Relativity Transformations. However this is not so-there exist an exact linear mapping between Galilean Relativity and Special Relativity (SR), differing only by definitions of space and time coordinates (Cahill, 2008). This implies that the so-called Special Relativity (SR) relativistic effects are not actual dynamical effects-they are purely

artifacts of a peculiar choice of space and time coordinates. In particular Lorentz symmetry is merely a consequence of this choice of space and time coordinates and is equivalent to Galilean symmetry. Nevertheless Lorentz symmetry remains valid, even though a local preferred frame of reference exists. Lorentz Relativity, however, goes beyond Galilean Relativity in that the limiting speed of systems wrt to the local space causes various so-called relativist effects, such as length contractions and clock dilations.

The Euler covariant constituent acceleration $a(r,t)$ of space is then defined by:

$$a = \lim_{\Delta t \rightarrow 0} \frac{v(r + v(r,t)\Delta t, t + \Delta t) - v(r,t)}{\Delta t} \\ = \frac{\partial v}{\partial t} + (v \cdot \nabla)v$$

Which describes the acceleration of a constituent element of space by tracking its change in velocity. This means that space has a (quantum) structure that permits its velocity to be defined and detected, which experimentally has been done. We assume here that the flow has zero vorticity $\nabla \times v = 0$ and then the flow is determined by a scalar function $v = \nabla u$. We then need one scalar equation to determine the space dynamics, which we construct by forming the divergence of a . The inhomogeneous term then determines a dissipative flow caused by matter, expressed as a matter density and where the coefficient turns out to be Newton's gravitational constant:

$$\nabla \cdot \left(\frac{\partial v}{\partial t} + (v \cdot \nabla)v \right) = -4\pi G \rho(r,t)$$

Note that even a time independent matter density or even the absence of matter can be associated with a time-dependent flow. In particular this dynamical space in the absence of matter has an expanding universe solution. Substituting the Hubble form $v(r, t) = H(t)r$ and then using $H(t) = a(t)/a(t)$, where $a(t)$ is the scale factor of the universe, we obtain the solution $a(t) = t/t_0$, where t_0 is the age of the universe, since by convention $a(t_0) = 1$. Then computing the magnitude-redshift function $\mu(z)$, we obtain excellent agreement with the supernova data and without the need for 'dark matter' nor 'dark energy' (Cahill and Rothall, 2012).

This equation follows essentially from covariance and dimensional analysis. For a spherically symmetric

matter distribution, of total mass M and a time-independent spherically symmetric flow we obtain from the above and external to the sphere of matter, the acceleration of space Equation 50:

$$v(r) = -\hat{r}\sqrt{\frac{2GM}{r}}, \text{ giving } a(r) = -\frac{GM}{r^2}\hat{r} \quad (50)$$

Which is the inverse square law. Newton applied such an acceleration to matter, not space and which Newton invented directly by examining Kepler's planetary motion laws, but which makes no mention of what is causing the acceleration of matter, although in a letter in 1675 to Oldenburg, Secretary of the Royal Society and later to Robert Boyle, he speculated that an undetectable ether flow through space may be responsible for gravity. Here, however, the inverse square law emerges from the Euler constituent acceleration, which imposes a space self-interaction. At the surface of the earth the in-flow speed is 11 km s^{-1} and the sun in-flow speed at 1AU is 42 km s^{-1} , with both detected (Cahill, 2009b).

While the above 3-space dynamical equation followed from covariance and dimensional analysis, this derivation is not complete yet. One can add additional terms with the same order in speed and spatial derivatives and which cannot be a priori neglected. There are two such terms, as in Equation 51:

$$\nabla \cdot \left(\frac{\partial v}{\partial t} + (v \cdot \nabla)v \right) + \frac{5\alpha}{4}((tr D)^2 - tr(D^2)) + \dots = -4\pi G\rho \quad (51)$$

where, $D_{ij} = \partial v_i / \partial x_j$. However to preserve the inverse square law external to a sphere of matter, when the matter is stationary, asymptotically, wrt space, the two terms must have coefficients α and $-\alpha$ as shown. Here α is a dimensionless space self-interaction coupling constant, which experimental data reveals to be, approximately, the fine structure constant, $\alpha = e^2/\hbar c$, (Cahill, 2005a; 2006c; 2009b) (Rothall and Cahill, 2013). The ellipsis denotes higher order derivative terms with dimensioned coupling constants, which come into play when the flow speed changes rapidly wrt separation. However the observed dynamics of stars and gas clouds near the centre of the Milky Way galaxy has revealed the need for such a term and we find that the space dynamics then requires an extra term:

$$\nabla \cdot \left(\frac{\partial v}{\partial t} + (v \cdot \nabla)v \right) + \frac{5\alpha}{4}((tr D)^2 - tr(D^2)) + \delta^2 \nabla^2((tr D)^2 - tr(D^2)) + \dots = -4\pi G\rho$$

where, δ has the dimensions of length and appears to be a very small Planck-like length, (Cahill and Kerrigan, 2011). This then gives us the dynamical theory of 3-space. It can be thought of as arising via a derivative expansion from a deeper theory, such as a quantum foam theory, (Cahill, 2005a). Note that the equation does not involve c , is non-linear and time dependent and involves non-local direct interactions. Its success implies that the universe is more connected than previously thought. Even in the absence of matter there can be time-dependent flows of space. To test this theory we need to determine how quantum matter and EM radiation respond to this dynamical space. We note immediately that this dynamics is very rich in that various new phenomena emerge and which have been observed and which do not occur in Newtonian gravity, which is a linear theory, nor in its relativistic generalisation, General Relativity (GR), with both being one-parameter theories, G : Essentially GR is flawed by the assumption that GR must reduce to Newtonian gravity in the non-relativistic low-mass limit. The extended dynamics, above, has the scale factor $a(t) = (t/t_0)^{1/(1+5\alpha/2)}$, which has a singularity at $t = 0$, giving rise to an intrinsic inflationary epoch. In GR inflation is phenomenologically introduced by means of an *ad hoc* inflation field.

1.12. Quantum Matter and 3-Space Emergent Gravity

We now derive, uniquely, how quantum matter responds to the dynamical 3-space. This gives the 1st derivation of the phenomenon of gravity and reveals this to be a quantum matter wave refraction effect. For a free-fall quantum system with mass m the Schrodinger equation is uniquely generalized (Cahill, 2006c), with the new terms required to maintain that the motion is intrinsically wrt the 3-space and not wrt the embedding space and that the time evolution is unitary:

$$i\hbar \frac{\partial \psi(r,t)}{\partial t} = -\frac{\hbar^2}{2m} \nabla^2 \psi(r,t) - i\hbar \left(v \cdot \nabla + \frac{1}{2} \nabla \cdot v \right) \psi(r,t)$$

The space and time coordinates $\{t, x, y, z\}$ ensure that the separation of a deeper and unified process into different classes of phenomena here a dynamical 3-space

(quantum foam) and a quantum matter system, is properly tracked and connected. As well the same coordinates may be used by an observer to also track the different phenomena. A quantum wave packet propagation analysis gives the matter acceleration $g = d^2\langle r \rangle / dt^2$ induced by wave refraction to be:

$$g = \frac{\partial v}{\partial t} + (v \cdot \nabla)v + (\nabla \times v) \times v_R + \dots$$

$$v_R(r_0(t), t) = v_0(t) - v(r_0(t), t)$$

where, v_R is the velocity of the wave packet relative to the 3-space and where v_0 and r_0 are the velocity and position relative to the observer. The last term generates the Lense-Thirring effect as a vorticity driven effect. In the limit of zero vorticity we obtain that the quantum matter acceleration is the same as the 3-space acceleration: $g = a$. This confirms that the new physics is in agreement with Galileo's observations that all matter falls with the same acceleration. Using arcane language this amounts to a derivation of the Weak Equivalence Principle.

Significantly the quantum matter 3-space-induced 'gravitational' acceleration also follows from maximising the elapsed proper time wrt the quantum matter wave-packet trajectory $r_0(t)$, (Cahill, 2005a) Equation 52:

$$\tau = \int dt \sqrt{1 - \frac{v_R^2(r_0(t), t)}{c^2}} \tag{52}$$

Which entails that matter has a maximum speed of c wrt to space and not wrt an observer. This maximisation ensures that quantum waves propagating along neighbouring paths are in phase - the condition for a classical trajectory. This gives Equation 53:

$$g = \frac{\partial v}{\partial t} + (v \cdot \nabla)v + (\nabla \times v) \times v_R$$

$$- \frac{v_R}{1 - \frac{v_R^2}{c^2}} \frac{1}{2} \frac{d}{dt} \left(\frac{v_R^2}{c^2} \right) \tag{53}$$

And then taking the limit $v_R/c \rightarrow 0$ we recover the nonrelativistic limit, above. This shows that (i) the matter 'gravitational' geodesic is a quantum wave refraction effect, with the trajectory determined by a Fermat maximum proper-time principle and (ii) that quantum systems undergo a local time dilation effect. The last,

relativistic, term generates the planetary precession effect. If clocks are forced to travel different trajectories then the above predicts different evolved times when they again meet-this is the Twin Effect, which now has a simple and explicit physical explanation-it is an absolute motion effect, meaning motion wrt space itself. This elapsed proper time expression invokes Lorentzian relativity, that the maximum speed is c wrt to space and not wrt the observer, as in Einstein SR. The differential proper time (52) has the form:

$$c^2 d\tau^2 = c^2 dt^2 - (dr - v(r, t)dt)^2 = g_{\mu\nu} dx^\mu dx^\nu$$

Which defines an induced metric for a curved spacetime manifold. However this has no ontological significance and the metric is not determined by GR.

1.13. Electromagnetic Radiation and Dynamical Space

We must generalise the Maxwell equations so that the electric and magnetic fields are excitations within the dynamical 3-space and not of the embedding space. The minimal form in the absence of charges and currents is:

$$\nabla \times E = -\mu_0 \left(\frac{\partial H}{\partial t} + v \cdot \nabla H \right), \quad \nabla \cdot E = 0$$

$$\nabla \times H = -\epsilon_0 \left(\frac{\partial E}{\partial t} + v \cdot \nabla E \right), \quad \nabla \cdot H = 0$$

Which was first suggested by (Hertz, 1890), but with v then being only a constant vector field and not interpreted as a moving space effect. As easily determined the speed of EM radiation is now $c = 1 / \sqrt{\mu_0 \epsilon_0}$ with respect to the 3-space and not wrt an observer in motion through the 3-space. The (Michelson and Morley 1887) experiment 1st detected this anisotropy effect, as have numerous subsequent experiments. A time dependent and/or inhomogeneous velocity field causes the refraction of EM radiation. This can be computed by using the Fermat least-time approximation-the opposite of that for quantum matter. This ensures that EM waves along neighbouring paths are in phase. Then an EM ray path $r(t)$ is determined by minimising the elapsed travel time:

$$T = \int_{s_i}^{s_f} \frac{ds \left| \frac{dr}{ds} \right|}{|c \hat{v}_R(s) + v(r(s), t(s))|}$$

With $v_r = \frac{dr}{dt} - v(r(t), t)$ by varying both $r(s)$ and $t(s)$, finally giving $r(t)$. Here s is an arbitrary path parameter and $c\bar{v}_r$ is the velocity of the EM radiation wrt the local 3-space, namely c . The denominator is the speed of the EM radiation wrt the observer's Euclidean spatial coordinates. This equation may also be used to calculate the gravitational lensing by black holes, filaments, (Cahill, 2011b) and by ordinary matter, using the appropriate 3-space velocity field. It produces the measured light bending by the sun. In particular galactic lensing agrees with observational data and does not require "dark matter".

1.14. Gravitational Wave Reverberations

Analysis of Bore Hole g anomaly data revealed that is the fine structure constant (Cahill, 2005a; 2006c; 2009b; Rothall and Cahill, 2013). The additional dynamics explains the "dark matter" effects and so may be referred to as the dark matter term Equation 54:

$$\rho_{DM}(r, t) = \frac{5\alpha}{16\pi G} ((tr D)^2 - tr(D^2)) \quad (54)$$

where, by Equation 55:

$$\nabla \cdot g = \nabla \cdot \left(\frac{\partial v}{\partial t} + \nabla \left(\frac{v^2}{2} \right) \right) = -4\pi G (\rho_M + \rho_{DM}) \quad (55)$$

We now demonstrate that gravitational waves incoming on, say, a star or planet develop reverberations, in which the wave generates following copies of itself. For numerical accuracy in solving for time dependent effects in (55), we assume a spherically symmetric incoming wave, which is clearly unrealistic and so find numerical solutions by using the ansatz $v(r, t) = v(r) + w(r, t)$, where $v(r) \sim 1/\sqrt{r}$ is the static in-flow from (50), applicable outside of the star/planet and so ignoring the galactic background flow and where $w(r, t)$ is the wave effect, with the initial wave $w(r, 0)$ having the form of a pulse, as shown in Fig. 35, where the time evolution of $w(r, t)$ is also shown. We see that the initial pulse develops following copies of itself. This is a direct consequence of the non-linearity of (51).

These reverberations are detectable in EM speed anisotropy experiments. However because the 3-space is fractal, as illustrated in Fig. 20 the reverberations are expected to be complex. As well all systems would generate reverberations, from planets, moons, sun and the

galaxy. The timescale for such reverberations would vary considerably. As well as being directly observable in EM anisotropy and gravitational wave detectors, these reverberations would affect, for example, nuclear decay rates, as the magnitude of the 3-space fractal structure is modulated by the reverberations and this fractal structure will stimulate nuclear processes. Patterns in the decay rates of nuclei have been observed by (Shnoll *et al.*, 2000; Shnoll, 2012) with periodicities over many time scales.

1.15. Shnoll Reaction Rate Effects

For over half a century Simon Shnoll has studied the non-Poisson rate-scatter anomalies in various phenomena such as biological and chemical reactions, radioactive decay, photodiode current leakage and germanium semiconductor noise. An example of this is Fig. 36, which shows a layered histogram of some 352,980 successive measurements of the decay rate of ^{239}Pu source undertaken by Shnoll between May 28-June 01, 2004. The layer lines taken every 6000 successive measurements show a fine structure which builds up over time instead of cancelling out as in the case of a typical random or Poisson distribution. This suggests that the radioactivity of ^{239}Pu takes on discrete (preferred) values and is not completely random. Shnoll found that the shapes of histograms from either the same or different experiments correlated via both absolute (same time) and local (time delay due to Earth's rotation) time synchronism and that the phenomenon causing this had a fractal nature. Shnoll attributed the cause of this to cosmophysical factors, i.e., inhomogeneities in the "spacetime continuum". These inhomogeneities are "caused by the movement of an object in the inhomogeneous gravitational field", e.g., as the Earth rotates/orbits the Sun, as the moon orbits the Earth. While these inhomogeneities were not characterised by Shnoll there is a remarkable amount of evidence supporting this conclusion.

An alternative model of reality leads to a description of space which is dynamic and fractal. The RF coaxial cable propagation experiment can be used to characterise gravitational waves. However the resolution of the data in the coaxial cable experiment proved to be insufficient to study changes in histogram shapes. It is reported here that a newer technique which studies the non-Poisson characteristics of the current fluctuations in zener diodes and may be used to study gravitational waves. This technique allows for faster recording of data (every second instead of every 5 sec) and used much higher digital resolution.

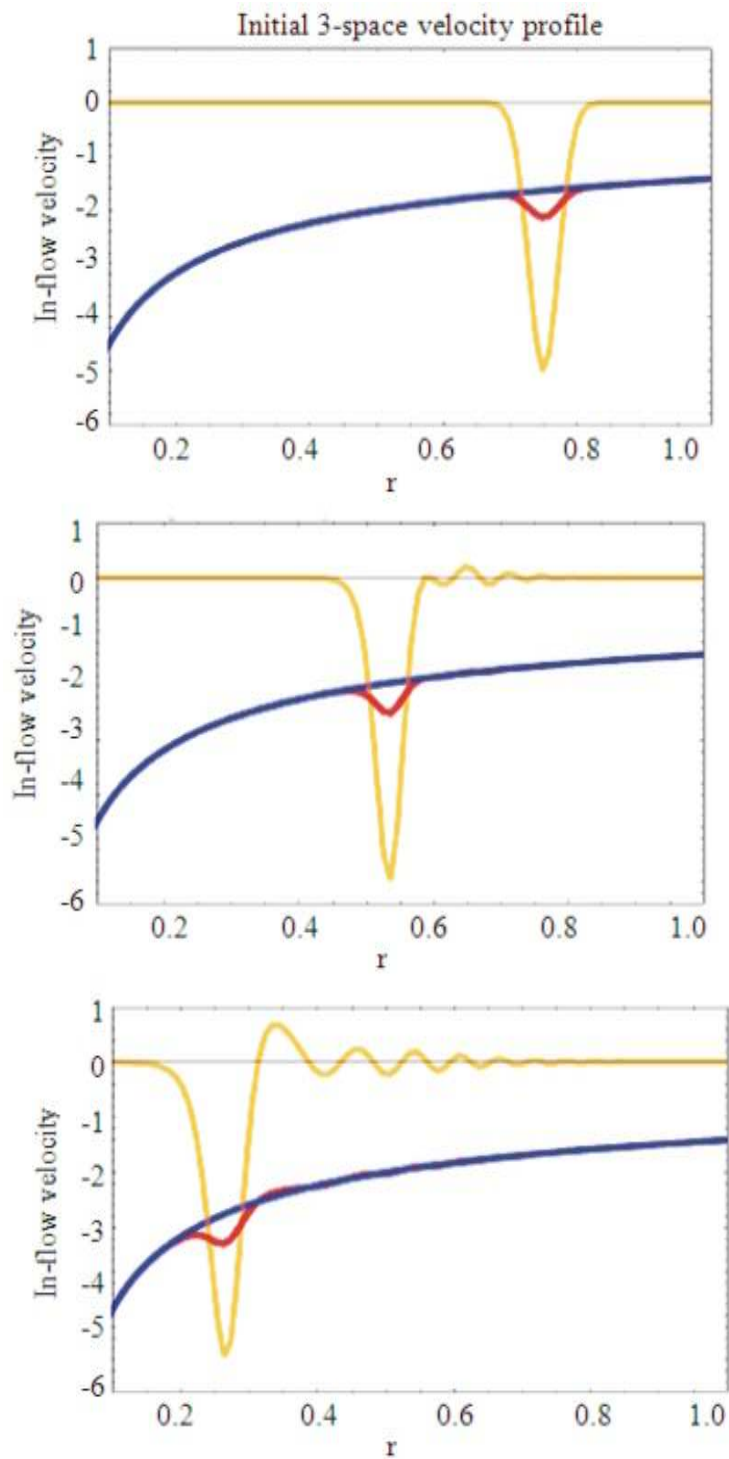


Fig. 35. Inflowing 3-space perturbation $w(r,t)$ (red) and un-perturbed inflow $v(r)$ blue velocity profiles outside a mass, with the waveform $w(r,t)$ also shown magnified (yellow), at later times

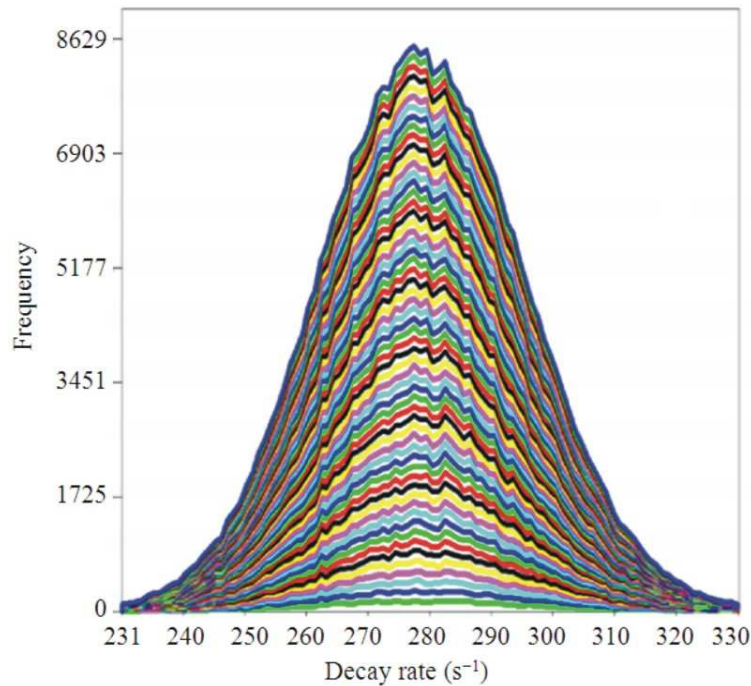


Fig. 36. Non-Poisson distribution of 352,980 measurements of ^{239}Pu α decay by Shnoll performed in 2004, **Fig. 2-2** of (Shnoll, 2012). The layered histograms are taken every 6000 measurements. The x-axis denotes the number of decay events per second and the y-axis is the frequency of measurements

An alternative explanation of the Shnoll effect has been proposed using the dynamical 3-space theory; see Process Physics (Cahill, 2005a). This arose from modeling time as a non-geometric process, having an emergent fractal space and time as separate phenomena and leads to a description of space which is dynamic and fractal.

A recent experiment uses the current fluctuations in a reverse biased zener diode circuit (Rothall and Cahill, 2014). This detector exploits the discovery that the electron tunneling current is not random, but caused by gravitational waves; namely fluctuations/turbulence in the passing dynamical 3-space. A Fast Fourier Transform of the zener diode data was taken to remove low frequency artefacts and then a histogram taken of the resultant 376,101 measurements (after inverse FFT) to generate the layered histogram plot shown in **Fig. 37**. Layer lines are inserted every 6100 measurements to show a comparison with the Shnoll plot in **Fig. 36 and 37** is remarkably comparable to **Fig. 36**, showing that the Shnoll effect is also present in zener diode

experiments. The structure observed appears to build up over time instead of cancelling out and is also found to persist regardless of the time scale used for the phase difference, suggesting that the phenomenon causing this has a fractal nature. If this is indeed caused by a dynamical and fractal 3-space then the persisting structure observed in **Fig. 36 and 37** correspond to regions of space passing the Earth that have preferred/discrete velocities and not random ones, as randomly distributed velocities would result in a Poisson distribution, i.e., no features. A likely explanation for this is that the gravitational waves propagating in the 3-space inflow of the Earth or Sun could become phase locked due to the relative locations of massive objects. This would cause reverberation effects, i.e., regions of space which have the same speed and direction, which then repeat over time. The reverberations would be detectable in many other experiments such as EM anisotropy, radiation decay, semiconductor noise generation and could in the future be used to further characterise the dynamics of space.

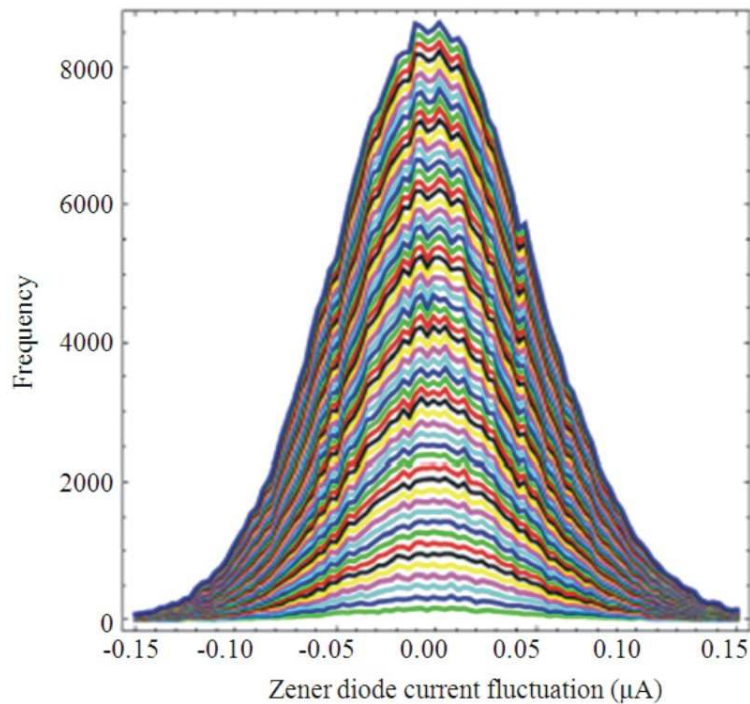


Fig. 37. Non-Poisson distribution of 376,101 measurements of zener diode current fluctuation (μA) observed from 20-27 Aug. 2013 in Adelaide. The layered histograms are taken every 6100 measurements to show a comparison with that of **Fig. 36**. The Zener diode fluctuations are known to be produced by gravitational waves: The fluctuations/turbulence in the flow of space. We thus infer that the decay rate fluctuations are also gravitational wave effects

2. CONCLUSION

We enumerate the many developments reported herein:

- Light speed is anisotropic, as reported in many experiments over the last 125 years
- The anisotropy is large, being 500 km s^{-1} , with RA = 5h, Dec. = -80°S . This is $>1/1000$ of the speed of light
- The anisotropy appears to be related to the flow of space in the Milky Way galaxy and the local cluster
- A variety of experimental techniques all agree: Gasmode Michelson interferometer, RF coaxial cables, optical fiber Michelson interferometer, optical fiber RF coaxial cables, spacecraft earth-flyby Doppler shifts, dual RF coaxial cables, zener diode quantum detectors and others not reviewed here
- All experiments have detected significant levels of turbulence/fluctuations in the anisotropy experiments: Gravitational waves
- The gravitational waves have two characteristics: An instantaneous action-at-a-distance effect and wave-like fluctuations propagating with the speed of the spatial flow
- Resonant bar detectors detected gravitational wave effects, including waves generated by earth vibrations
- The anisotropy data contradicts the key assumption of Special Relativity: That the speed of light/EM waves is invariant wrt any observer (in vacuum)
- Vacuum mode Michelson interferometers have zero sensitivity to light speed anisotropy and so also gravitational waves, as they have indeed reported
- Starting the modelling of space and time anew from the anisotropy of light speed a new dynamical theory of space is easily derived
- Gravity is an emergent phenomena, when using the generalized quantum wave equations-essentially a quantum wave refraction process
- The Hertz generalisation of Maxwell equations (without charges and currents) explains the anisotropy effect, as well as various EM lensing effects
- The space fluctuations drive the Shnoll effect, namely non-Poisson fluctuations in various quantum decay rates
- The dynamical 3-space equations have black hole solutions and without requiring in-fall of matter

- The dynamical 3-space equations successfully describe the bore-hole g anomaly, the flat rotation curves for spiral galaxies and the expansion of the universe, without requiring “dark matter” nor “dark energy”

3. ACKNOWLEDGEMENT

This report is from the Flinders University Gravitational Wave Detector Project, funded by an Australian Research Council Discovery Grant: Development and Study of a New Theory of Gravity. Thanks to GCP and its director Dr Roger Nelson for the public availability of extensive and valuable data from the REG international network: <http://teihard.global-mind.org/>. Thanks to Dr David Brotherton-Ratclie who played a key role in the discovery of the zener diode effect by operating the DSO in London.

4. REFERENCES

- Amaldi, E., E. Coccia, S. Frasca, I. Modena and P. Rapagnani *et al.*, 1981a. Background of gravitational-wave antennas of possible terrestrial origin-I. *Nuovo Cimento*, 4: 295-308. DOI: 10.1007/BF02574722
- Amaldi, E., S. Frasca, G.V. Pallottino, G. Pizzella and P. Bonifazi, 1981b. Background of gravitational-wave antennas of possible terrestrial origin-I. *Nuovo Cimento*, 4: 309-323. DOI: 10.1007/BF02574723
- Anderson, J.D., J.K. Campbell, J.E. Ekelund, J. Ellis and J.F. Jordan, 2008. Anomalous orbital-energy changes observed during spacecraft flybys of earth. *Phys. Rev. Lett.*, DOI: 10.1103/PhysRevLett.100.091102
- Braximaier, C., H. Muller, O. Pradl, J. Mlynek and O. Peters, 2001. Tests of relativity using a cryogenic optical resonator. *Phys. Rev. Lett.*, 88: 010401-010401. DOI: 10.1103/PhysRevLett.88.010401
- Cahill, R.T., 2006a. A new light-speed anisotropy experiment: Absolute motion and gravitational waves detected. *Progress Phys.*, 4: 73-92.
- Cahill, R.T., 2006b. Absolute motion and gravitational wave experiment results. *Proceedings of the Contribution to Australian Institute of Physics National Congress, (PNC' 06), Brisbane.*
- Cahill, R.T., 2006c. Dynamical fractal 3-space and the generalised schrodinger equation: Equivalence principle and vorticity effects. *Progress Phys.*, 1: 27-34.
- Cahill, R.T., 2006d. The roland de witte 1991 experiment. *Progress Phys.*, 3: 60-65.
- Cahill, R.T., 2006e. 3-Space inflow theory of gravity: boreholes, black holes and the fine structure constant. *Progress Phys.*, 2: 9-16.
- Cahill, R.T., 2007. Optical-fiber gravitational wave detector: Dynamical 3-space turbulence detected. *Progress Phys.*, 4: 63-68.
- Cahill, R.T. and D. Brotherton, 2011. Experimental investigation of the Fresnel drag effect in RF coaxial cables. *Progress Phys.*, 1: 041-48.
- Cahill, R.T. and D. Kerrigan, 2011. Dynamical space: Supermassive black holes and cosmic filaments. *Progress Phys.*, 4: 79-82.
- Cahill, R.T. and F. Stokes, 2008. Correlated detection of submhz gravitationalwaves by two optical-fiber interferometers. *Progress Phys.*, 2: 103-110.
- Cahill, R.T. and K. Kitto, 2003. Michelson-morley experiments revisited. *Apeiron*, 10: 104-117.
- Cahill, R.T. and D. Rothall, 2012. Discovery of uniformly expanding universe. *Progress Phys.*, 1: 63-68.
- Cahill, R.T. and S. Deane, 2013. Dynamical 3-space gravitational waves: Reverberation effects. *Progress Phys.*, 2: 9-11.
- Cahill, R.T., 2005a. *Process Physics: From Information Theory to Quantum Space and Matter*. 1st Ed., Nova Science Publishers, New York, ISBN-10: 1594543003. pp: 215
- Cahill, R.T., 2005b. The Michelson and Morley 1887 experiment and the discovery of absolute motion. *Progress Phys.*, 3: 25-29.
- Cahill, R.T., 2008. Unravelling Lorentz covariance and the space-time formalism. *Progress Phys.*, 4: 19-24.
- Cahill, R.T., 2009a. The Dynamical Velocity Superposition Effect in the Quantum-Foam Theory of Gravity. In: *Relativity, Gravitation, Cosmology: New Developments*, Dvoeglazov, V. (Ed.), Nova Science Pub., New York, ISBN-10: 1606923331, pp: 113-133.
- Cahill, R.T., 2009b. Dynamical 3-Space: A Review. In: *Ether Space-time and Cosmology: New Insights into a Key Physical Medium*, Duy and Levy (Eds.), Apeiron, ISBN-10: 978-0-9732911-8-6, pp: 135-200.
- Cahill, R.T., 2009c. Combining NASA/JPL one-way optical-fiber light speed data with spacecraft earth-flyby doppler-shift data to characterise 3-space flow. *Progress Phys.*, 4: 50-64.
- Cahill, R.T., 2011a. Dynamical 3-Space: Emergent Gravity. In: *Should the Laws of Gravity be Reconsidered?* Munera, H.A. (Ed.), Apeiron, Montreal, ISBN 978-0-9864926-5-5, pp: 363-376.

- Cahill, R.T., 2011b. Dynamical 3-space: Cosmic filaments, sheets and voids. *Progress Phys.*, 2: 44-51.
- Cahill, R.T., 2012a. Characterisation of low frequency gravitational waves from dual RF coaxial-cable detector: Fractal textured dynamical 3-space. *Progress Phys.*, 3: 3-10.
- Cahill, R.T., 2012b. One-way speed of light measurements without clock synchronization. *Progress Phys.*, 3: 43-45.
- Cahill, R.T., 2013a. Dynamical 3-space: Neo-Lorentz relativity. *Phys. Int.*, 4: 60-72. DOI: 10.3844/pisp.2013.60.72
- Cahill, R.T., 2013b. Nanotechnology quantum detectors for gravitational waves: Adelaide to London correlations observed. *Progress Phys.*, 4: 57-62.
- Cahill, R.T., 2014. Discovery of dynamical 3-space: Theory, experiments and observations-a review. *Am. J. Space Sci.*, 1: 77-93. DOI: 10.3844/ajssp.2013.77.93
- Collins, H., 2004. *Gravity's Shadow: The Search for Gravitational Waves*. 1st Edn., University of Chicago Press, Chicago, ISBN-10: 0226113795. pp: 864
- Einstein, A. 1905. Zur elektrodynamik bewegter Korper. *Annalen der Phys.*, 17: 891-921.
- Hertz, H., 1890. On the fundamental equations of electro-magnetics for bodies in motion. *Electric Waves*, Collection of Scientific Papers, Dover Pub., New York.
- Krisher, T.P., L. Maleki, G.F. Lutes, L.E. Primas and R.T. Logan *et al.*, 1990. Test of the isotropy of the one way speed of light using hydrogen-maser frequency standards. *Phys. Rev. D*, 42: 731-734. DOI: 10.1103/PhysRevD.42.731
- Lipa, J.A., J.A. Nissen, S. Wan, D.A. Stricker and D. Avalo, 2003. New limit on signals of lorentz violation in electrodynamics. *Phys. Rev. Lett.* DOI: 10.1103/PhysRevLett.90.060403
- Lorentz, H.A., 1904. Electromagnetic phenomena in a system moving with any velocity smaller than that of light. *Proceedings of the Royal Netherlands Academy of Arts and Sciences*, (AAS' 04).
- Masters, T.G. and R. Widmer, 1985. Free Oscillations: Frequencies and Attenuations. In: *Global Earth Physics, a Handbook of Physical Constants*, Ahrens I.J. (Ed.), AGU, pp: 104-125.
- Michelson, A.A. and E.W. Morley, 1887. On the relative motion of the earth and the Luminiferous ether. *Am. J. Sci.*, 34: 333-345. DOI: 10.2475/ajs.s3-34.203.333
- Miller, D.C., 1933. The Ether-Drift Experiment and the Determination of the Absolute Motion of the Earth. *Rev. Mod. Phys.*, 5: 203-242. DOI: 10.1103/RevModPhys.5.203
- Muller, H., S. Herrmann, A. Saenz and A. Peters, 2003a. Optical cavity tests of Lorentz invariance for the electron. *Phys. Rev. D*. DOI: 10.1103/PhysRevD.68.116006
- Muller, H., C. Braxmaier, S. Herrmann and A. Peters, 2003b. Electromagnetic cavities and Lorentz invariance violation. *Phys. Rev. D*. DOI: 10.1103/PhysRevD.67.056006
- Pound, R.V. and G.A. Rebka, 1960. Apparent weight of photons. *Phys. Rev. Lett.*, 4: 337-341. DOI: 10.1103/PhysRevLett.4.337
- Rothall, D.P. and R.T. Cahill, 2013. Dynamical 3-space: Black holes in an expanding universe. *Progress Phys.*, 4: 25-31.
- Rothall, D.P. and R.T. Cahill, 2014. Dynamical 3-space: Observing Gravitational wave fluctuations and the Shnoll effect using a Zener diode quantum detector. *Progress Phys.*, 10: 16-18.
- Shnoll, S.E., 2012. *Cosmophysical Factors in Stochastic Processes*. 1st Edn., American Research Press, Rehoboth, New Mexico, USA.
- Shnoll, S.E., T.A. Zenchenko, K.I. Zenchenko, E.V. Pozharskii and V.A. Kolombet *et al.*, 2000. Regular variation of the fine structure of statistical distributions as a consequence of cosmophysical agents. *Phys. Usp.*, s 43: 205-209. DOI: 10.1070/PU2000v043n02ABEH000669
- Weber, J., 1969. Evidence for discovery of gravitational radiation. *Phys. Rev. Lett.*, 22: 1320-1324. DOI: 10.1103/PhysRevLett.22.1320
- Weber, J., 1970. Anisotropy and polarization in the gravitational-radiation experiments. *Phys. Rev. Lett.*, 25: 180-184. DOI: 10.1103/PhysRevLett.25.180
- Weber, J., 1972. Computer analysis of gravitational radiation detector coincidences. *Nature*, 240: 28-30. DOI: 10.1038/240028a0
- Wolf, P., S. Bize, A. Clairon and G. Santarelli, 2004. Improved test of lorentz invariance in electrodynamics. *Phys. Rev. D*. DOI: 10.1103/PhysRevD.70.051902
- Wolf, P., S. Bize, A. Clairon, A.N. Luiten and G. Santarelli *et al.*, 2003. Tests of lorentz invariance using a microwave resonator. *Phys. Rev. Lett.* DOI: 10.1103/PhysRevLett.90.060402